FORMATION OF CARBON NANOSPRINGS VIA PRECURSOR CONSTRAINED FIBER MICROBUCKLING

A Thesis

by

SUMIT

Submitted to the Office of Graduate and Professional Studies of
Texas A&M University
in partial fulfillment of the requirements for the degree of

MASTER OF SCIENCE

Chair of Committee,	Mohammad Naraghi
Committee Members,	Vikram Kinra
	Matt Pharr
Head of Department,	Rodney Bowersox

December 2019

Major Subject: Aerospace Engineering

ABSTRACT

Flexible carbon nanosprings and wavy nanofibers can be used in micro and nanoelectromechanical system devices, deployable structures, flexible displays, energy storage, catalysis, nanocomposites and a multitude of other uses. A novel method to produce wavy and helical carbon nanofibers (CNFs) is presented here. The CNFs with controlled geometry were fabricated via pyrolysis of electrospun polyacrylonitrile (PAN) nanofibers as the precursor. The waviness/helicity of nanofibers was achieved by subjecting the precursor nanofibers to constraint buckling inside a thermally shrinking matrix. The much higher tendency of the matrix to shrink, compared to PAN nanofibers, was achieved by controlling the microstructure and crystallinity of the precursors. The formation of the wavy/helical geometry was explained quantitatively via mechanistic models, by minimizing the total mechanical energy stored in the PAN-matrix system during the matrix shrinkage. Despite its simplicity in considering elastic deformations only, the model provided reasonably quantitative matching with the experiments. Compared to existing methods in generating wavy/helical nanofibers, such as chemical vapor deposition growth methods, our method provides a more controllable geometry which is suitable for large scale production of aligned buckled CNFs.

DEDICATION

To my parents, friends, teachers throughout my years of education.

ACKNOWLEDGEMENTS

I would like to sincerely express my thanks and gratitude to my advisor, Dr. Mohammad Naraghi for his expertise, encouragement, understanding and support during my MS study period in Texas A&M University, which makes it to be an invaluable experience in my life. I would also like to thank my committee members, Dr. Vikram Kinra and Dr. Matt Pharr for their kindly support and valuable feedbacks.

The use of the TAMU Materials Characterization Facility and Soft Matter Facility is also acknowledged. I am grateful to Jizhe Cai, Yijun Chen, Kai Morikawa, Jamshid Kavosi, Aniruddh Vashisth & Ahmad Amiri and all other members from our group for their helps during my graduate study, research and dissertation writing.

Lastly, my deepest appreciation belongs to my family, for their continued patience, understanding and support.

CONTRIBUTORS AND FUNDING SOURCES

Contributors

This work was supervised by a thesis committee consisting of Professor Mohammad Naraghi and Professor Vikram Kinra of the Department of Aerospace Engineering and Professor Matt Pharr of the Department of Mechanical Engineering.

All other work conducted for the thesis (or) dissertation was completed by the student independently.

Funding Sources

This work was also made possible in part by the support from Air Force Office of Scientific Research, under the award number FA9550-15-1-0170. The FE-SEM acquisition was supported by the NSF grant DBI-0116835, the VP for Research Office, and the TX Eng. Exp. Station. Its contents are solely the responsibility of the authors and do not necessarily represent the official views of the Air Force Office of Scientific Research.

NOMENCLATURE

λ	Hot drawing ratio
A	Amplitude
H	Wavelength or pitch
R	Radius of Curvature
r	Helix radius
n	Mode shape
M	Bending moment
E	Young's modulus
G	Shear modulus
I	Moment of inertia
J	Polar moment of inertia
α	Ratio of fiber end to end distance after and before shrinkage
T	Torque
ϕ	Angle of twist
PAN	Polyacrylonitrile
PMMA	Poly (methyl methacrylate)
DMF	Dimethylformamide
DCM	Dichloromethane
MEMS	Micro electromechanical systems

NEMS	Nano electromechanical systems
DMA	Dynamic mechanical analysis
SEM	Scanning electron microscope
CMC	Carbon microcoils
CVD	Chemical vapor deposition
CNF	Carbon nanofiber

TABLE OF CONTENTS

Page

LIST OF FIGURES

Page

LIST OF TABLES

Page

1 INTRODUCTION & SIGNIFICANCE*

Springs and coils are essential structural and electromagnetic components with a wide range of applications. From a structural standpoint, the ability of a spring to elastically undergo large relative dimensional changes at considerably lower material strains facilitated by its peculiar shape has made springs an important component in shock absorbers, load cells, clocks, computer keyboards, engines, deployable structures and in a host of other equipment [1]. With the advance of nanotechnology, now it is also possible to synthesize and manipulate springs at the nanoscale, often known as nanosprings and nanocoils. These nanostructures possess all the essential qualities of a larger spring, as the ratio of the relative dimensional changes of a spring over material strains is size-invariant. For instance, Chen et al [2] carried out tensile tests on a single carbon nanocoil synthesized by chemical vapor synthesis (CVD) with the help of an iron-coated indium tin oxide (ITO) thin film by clamping it in between two atomic force microscope (AFM) cantilever tips and leading to relative stretch of around 42%, the nanocoil behaved like an elastic spring with a measured spring constant of 0.12 N/m without any observed plastic deformation. This is significantly higher than 1-2% strain to failure of straight carbon nanofibers. In particular, however, reducing the dimensions of coils to the nanoscale may further broaden their application by benefiting from the mechanical and material size effects observed in nanomaterials.

---

*Portions of this chapter are reprinted or adapted with permission from [67], Sumit Khatri, Jizhe Cai and Mohammad Naraghi, "Formation of wavy carbon nanofibers and nanocoils via precursor constrained microbuckling." Journal of the Mechanics and Physics of Solids, Volume 134, 103763, 2020. Copyright [2019] by PERGAMON. Doi: https://doi.org/10.1016/j.jmps.2019.103763.

1.1 Literature Survey

A nanospring not only is load bearing building blocks in the microelectromechanical systems (MEMS) or nanoelectromechanical systems (NEMS) but can also serve as nanoscale sensors and actuators by combining the inherent flexibility of these nanostructures as a mechanism to transduce force to displacement while relying on with piezoresistance change of the structure to account for force and displacement in some cases [3-5]. Nanosprings can store mechanical energy and act as a load cell for nano-devices and also act as a nanoscale electromagnet or actuator by the induction of a magnetic field or via electric current [5-7]. One more exciting application of nanosprings is flexible electronics which demands not only flexibility but also electrical conductivity, for instance for stretchable displays [8], energy storage devices [9], robotics [10], sensors [11], membrane antennas for space-based radar, membrane solar arrays for space power systems, integral health monitoring sensors for membrane radars and solar sails [12, 13].

Stretchable conductors play an important role in fabricating stretchable electronics, which require highly stretchable components with robust electrical conductivity [14]. Nanocoils have been synthesized from a variety of materials including SiO_2 [15], SiC [16], $B_4\,C$ [17] via chemical vapor deposition (CVD), Si via the so-called glancing layer deposition [18], and polymers via bicomponent electrospinning [19]. Among different types of nanocoils, carbon nanocoils have shown a lot of potential, as they combine the benefits of the helical shape (such as high deformability) with high specific mechanical strength, high surface area, good electrical conductivity and thermal stability [20-33]. For instance, helical

“carbon microcoils” or CMCs synthesized by CVD technique have shown excellent elasticity, which can be extended and contracted by 3-15 times their original length, and as such can be used as reinforcement of composites. It is to be noted that while they were referred to as microcoils, they are sub-micron thick carbon strands in helical shapes. As such, they may be referred to as carbon nanocoils as well [34]. The helical shape not only controls the ratio of the overall relative deformation of spring to material strain, but these helical microcoils have been observed to more effective as structural reinforcement material in polymer composites such as low Young’s modulus epoxy resin than even carbon fibers. The polymer composites fabricated using these microcoils reveal minimal pull out failure due to mechanical interlocking with the surrounding polymer matrix, resisting pull out failure [35].

Carbon nanocoils have also been used as electrodes of lithium ion batteries. Carbon nanocoils offer a highly efficient Lithium ion storage for lithium ion batteries showcasing high rate capability as well as long term cyclic life. The excellent electromechanical performance is believed to be due to the nano size and the helical morphology. Enhanced lithium ion storage is due to higher specific surface area exhibited by nano scale which directly leads to better rate capability. While the flexibility offered by helical nanospring like structures results in optimal management of strains produced due to volumetric variation due to ion uptake-release cycles related to charging and discharging of cell respectively, which is the cause of excellent cyclic life and reliability [36]. Another application of carbon nanocoils is nanoscale magnetic sensors. As the carbon coils are

electrically conductive, they act as a solenoid coil which generates an electromotive force in the presence of a magnetic field, while passing a direct current through the coil results in measurable magnetic field around the structure. Due to the flexibility of these nanostructures, they can extend and contract many times the original length which affects the electrical parameters. The extension of these coils is highly sensitive to applied force and could be used to detect even relatively small loads of the order of milligrams. Thus opening doors for usage of these nanostructures as a nanoscale magnetic sensor or actuator [37-39]. Nanocoils are chiral materials due to their spring like morphology which is an important parameter in the microwave absorption materials. These chiral structures provide a chiral admittance while exhibiting the general parameters of permittivity and permeability observed in usual dielectric materials. The enhanced microwave absorption properties of carbon nanocoils is attributed to dielectric loss rather than the magnetic loss. Additionally, interfacial multipoles also help in efficient absorption of microwaves [40]. In addition, a rather long resistive element can be confined in a compact space by forming a helical shape. Thus, helicity is beneficial in enhancing microwave absorption in nanomaterials via dielectric/induction heating caused by alternating electric and magnetic fields [41-43].

The primary approach to fabricate helical and wavy carbon fibers has so far been catalytic chemical vapor deposition (CVD) [44-52] where these nanostructures are grown on metal catalytic particles while using a hydrocarbon as the source for the carbon. However, the growth mechanism of the helical structure in CVD is not well established, presenting a

roadblock in the fabrication of nanocoils with application-specific geometries and microstructure. Efforts have been made to address this gap. For instance, Wang et al. [53], studied the growth of helical carbon nanofibers using primary (Fe) and secondary (e.g., Sn) catalysis. Based on the variations of the helical angle, they provided a qualitative explanation for the growth of the structures based on the affinity of the nanostructure and the substrate. Despite the partial success in developing helical structures, their method led to a combination of helical and straight fibers, demanding further studies to predictably explain the growth mechanism. Moreover, this technique has lots of inherent limitations such as significant amount of catalyst residue, relatively lower product yield and alignment issues [54-56].

To address this processing gap, in this work we report a mechanics-based approach to fabricate CNFs with controllable waviness through carbonization of electrospun precursor nanofibers which are subjected to microbuckling inside a sacrificial matrix. Compared to the "bottom-up" method of production employed by CVD, electrospinning takes advantage of its "top-down" manufacturing process, which facilitates production, assemblage, and alignment [57, 58]. This study focuses on the fabrication, material properties and mechanics that leads to the formation of wavy carbon nanofibers, in order to establish the relationship between processing parameters and the resulting wavy fiber geometry. These fabrication-structure-properties relationships will help in designing a scalable methodology with full control of the final outcome in terms of geometry and properties.

1.2 Goals and Objective

Synthesis & characterization of carbon nanosprings by constrained microbuckling of precursor fiber in a sacrificial matrix and prediction of shape configuration & transition by mechanics based microbuckling model.

I. Fabrication of wavy carbon nanofibers via precursor fiber microbuckling inside a sacrificial PMMA matrix.

II. Establish the relationship between processing parameters and the resulting wavy fiber geometry.

III. Development of a mechanistic microbuckling model in elastic domain, by minimizing the total mechanical energy stored in the PAN-matrix system to predict the shape configuration and transition from one configuration to the other.

IV. Demonstrate fabrication-structure-properties relationships to help in designing a scalable methodology with full control of the final outcome in terms of geometry and properties.

2 EXPERIMENTAL PROCEDURE*

The wavy and helical CNFs were fabricated through thermal stabilization and carbonization of electrospun polyacrylonitrile (PAN) nanofibers as the precursor. Prior to pyrolysis, the semicrystalline PAN nanofiber precursors were subjected to hot drawing assisted microbuckling inside a sacrificial and thermally shrinking poly (methyl methacrylate) (PMMA) amorphous matrix to obtain the wavy or helical precursors.

Shape configuration of obtained buckled fibers was analyzed using SEM images and correlation between input parameters like hot drawing ratio and output parameters like wavelength, pitch, amplitude and helix radius was established. Thermomechanical characterization of pure PAN and PMMA films was carried out using dynamic mechanical analysis to ascertain the effect of temperature on mechanical behavior of materials involved.

2.1 Fabrication of PAN nanofiber ribbons and PAN/PMMA composites

Ribbons of PAN nanofibers as precursors of helical CNFs were fabricated by electrospinning. To this end, polyacrylonitrile (PAN) powder from Sigma Aldrich with a molecular weight of 150,000 g/mol was dissolved into dimethylformamide (DMF) to obtain a 12 wt. % solution (PAN in DMF).

*Portions of this chapter are reprinted or adapted with permission from [67], Sumit Khatri, Jizhe Cai and Mohammad Naraghi, "Formation of wavy carbon nanofibers and nanocoils via precursor constrained microbuckling." Journal of the Mechanics and Physics of Solids, Volume 134, 103763, 2020. Copyright [2019] by PERGAMON. Doi: https://doi.org/10.1016/j.jmps.2019.103763.

The feeding rate of the polymer solution during electrospinning was kept at 1.4 ml/h to achieve stable electrospinning jet. Highly aligned polymer nanofiber ribbon was obtained by using a rotating disk collector with a peak-up velocity of ~5.7 m/s which induces a partial chain alignment within individual nanofibers due to the mechanical force exerted on the collected fibers by rotating disc resulting elongation and shear force. The electrospinning voltage and distance were 18 kV and 20 cm, respectively. The whole setup for electrospinning was enclosed in a humidity chamber kept at constant relatively low humidity of ~ 25% with a temperature of ~ 23°C. Figure 1 shows the whole electrospinning setup.

The as-electrospun PAN nanofiber ribbons were dip-coated with PMMA by inserting them into an 8 wt.% solution of PMMA (from Sigma Aldrich with a molecular weight of 350000 g/mol) in dichloromethane (DCM) solution for 15 minutes and then drying to form a nanocomposite containing PAN nanofiber and PMMA matrix.

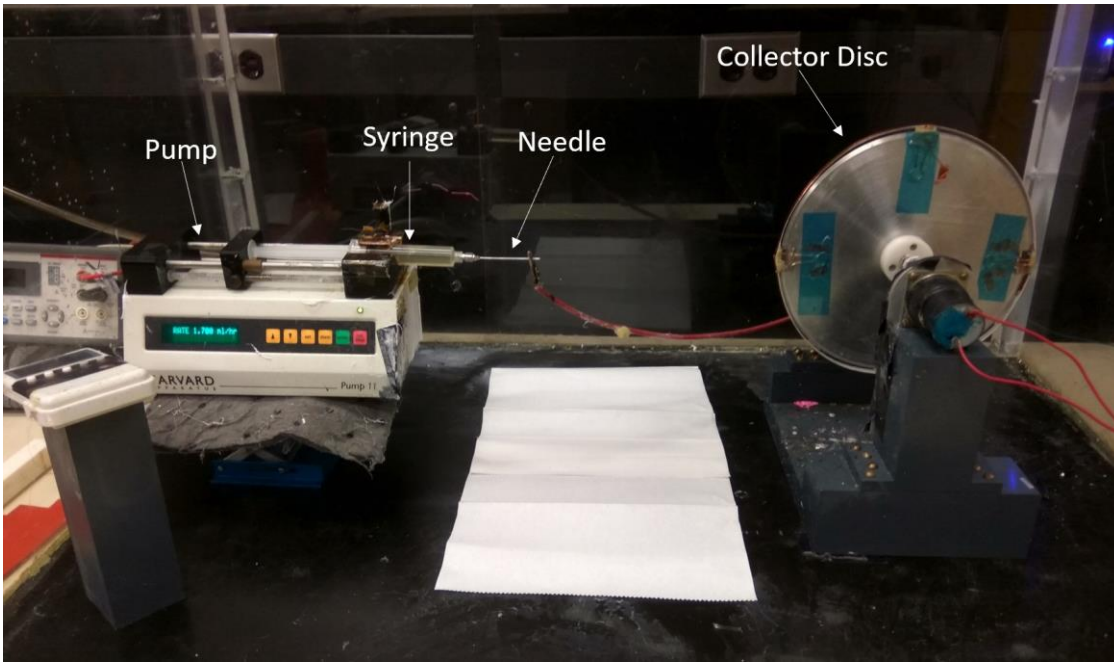

Figure 1. Electrospinning experimental setup with the pump, syringe, needle and the collector disc placed in a humidity-controlled chamber.

2.2 Enahnce Chain Alignment in Precursors via Hot Drawing

To further enhance the chain alignment, hot drawing is employed which is essentially a mechanical stretching at a temperature above the glass transition temperature of polymer. During hot drawing the free volume of the polymer chains is enhanced, resulting in increased chain mobility which in turn leads to uncoiling, stretching and alignment along the direction of applied load. The electrospun PAN/PMMA nanofiber ribbons were cut in to 2 cm long sample ribbons and subjected to hot drawing as follows. The as-spun PAN/PMMA composite ribbons were hot drawn at 135° C environment in an oven by hanging weights to them, inducing engineering stress of ~19 MPa. When the draw ratio (λ, the ratio of the final to initial length) reached the desired values of 3 (stretching from

initial length of 2 cm to 6 cm) and 5 (initial length of 2 cm to 10 cm), the stretched ribbons were cooled down to room temperature. Hot drawing plays a crucial role in fiber diameter, alignment, and crystallinity [57]. During the hot drawing process, due to the chain alignment and chain packing, the PAN nanofibers undergo drawing-induced crystallization [57], while the PMMA matrix remains largely amorphous.

2.3 Fabrication of carbon nanosprings

2.3.1 Heat Treatment

The PAN nanofibers were subsequently stabilized. To this end, the hot-drawn PAN/PMMA composite was thermally stabilized at 300° C in the presence of oxygen which results in the conversion of C ≡ N groups of PAN chains to C = N, forming a stable cyclic ladder-like structure [58]. Moreover, during the stabilization process, the entropic (mostly active in amorphous PMMA) and chemical reaction (mainly in stabilizing PAN) induce the shrinkage of hot-drawn PAN/PMMA composite.

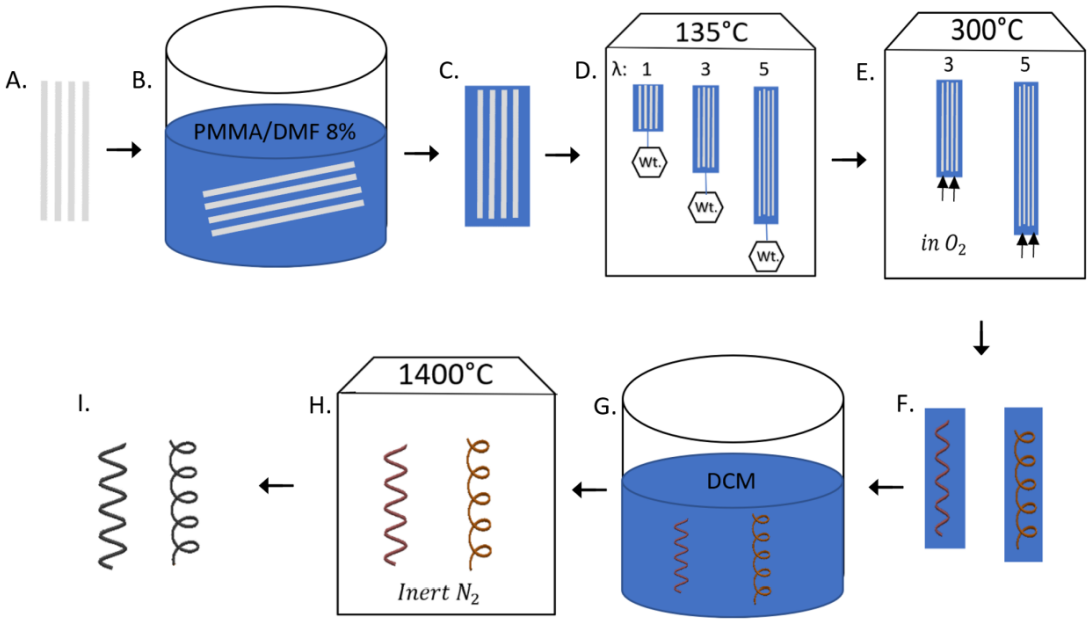

Figure 2. Schematic of manufacturing procedure: A) Electrospun PAN ribbon B) Dip coating with PMMA C) PAN/PMMA nanocomposite D) Hot drawing to stretch ratio (λ) 3 and 5 E) Entropic and chemically induced compression in stabilization F) Sinusoidal and helical PAN fibers in PMMA G) PMMA removal H) Carbonization I) Sinusoidal and helical carbon nanofibers (Reprinted with permission from [67]).

The shrinkage of the composite is dominated by the entropic forces within the PMMA, due to both its much larger relative mass and its amorphous structure which provides high mobility for PMMA chains. The PAN nanofibers accommodate the large relative shrinkage imposed on them by the matrix mainly via constraint buckling. Because of large compressive strains and condition of symmetry, the buckling under the constraint of surrounding PMMA matrix can result in either a planar wavy (sinusoidal) or a 3-dimensional helical buckling as readily observed in compressive buckling of a fiber in an elastomeric matrix [18, 59-62]. After the microbuckling of the PAN fibers due to thermal

shrinkage in the matrix, the deformed shape of the PAN nanofibers is fixed due to chemical crosslinks (cyclization). In the carbonization process, the PMMA phase will be fully decomposed and PAN nanofiber will be transferred to CNF. Carbonization is carried it at 1400°C in a nitrogen atmosphere in the tube furnace for 10 hours which enables the formation of turbostratic domains in the PAN nanofibers with the elimination of non-carbon atoms from the chains. Finally, we get ribbons of thousands of aligned wavy carbon nanofibers.

2.3.2 Entropic & Thermal Shrinkage

To evaluate the relative ability and tendencies of PAN nanofibers and PMMA matrix to shrink during thermal stabilization, pure PAN nanofiber ribbons, PMMA films, and PAN/PMMA ribbons were subjected to various degrees of hot-drawing and their shrinkage during subsequent heat treatments was measured, Figure 3. As shown in the figure, there are considerable differences between the shrinkage of PMMA films and PAN nanofiber ribbons. After hot-drawing to a draw ratio of 5, the matrix shrinks by ~60% at ~160 °C, compared to the small shrinkage of the PAN nanofiber ribbons (less than 10%). The small shrinkage of PAN nanofibers can be attributed to the hot-drawing induced crystallization in PAN nanofibers [57]. The crystalline domains serve as permanent anchor points within each PAN nanofiber, preventing considerable shape changes by entropic forces during thermal stabilization. In contrast, PMMA ribbons remain largely amorphous throughout the whole process, and the hot-drawing can induce chain alignment in PMMA, reducing the entropy of the matrix.

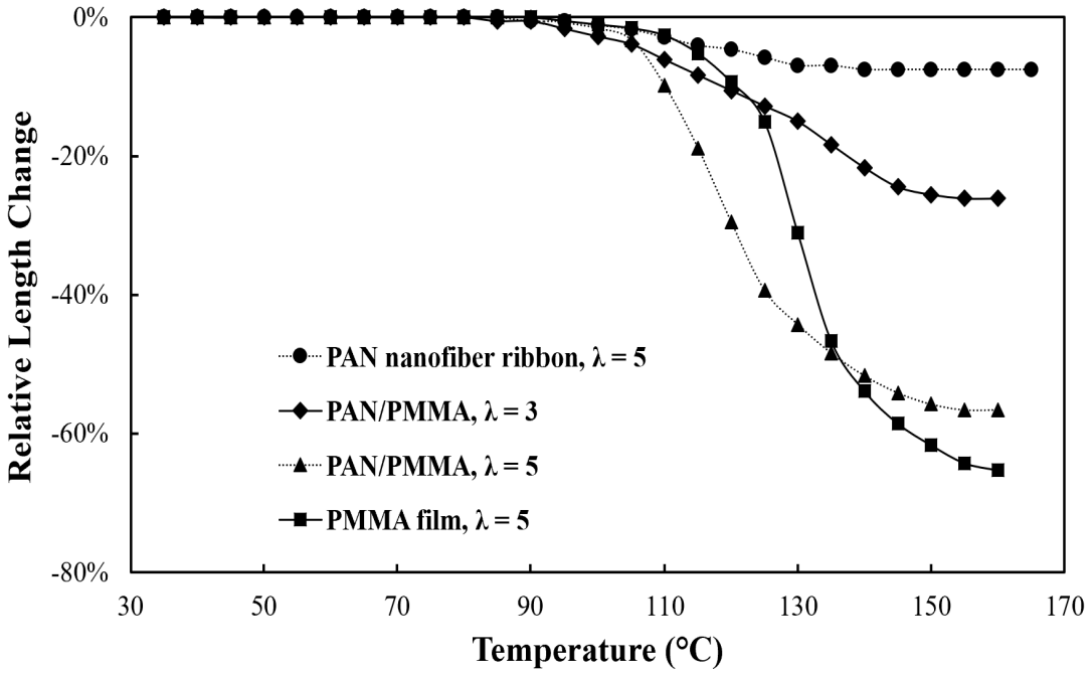

Figure 3. Stress-free relative change in length as a function of temperature for pure PAN nanofiber ribbons, PMMA films and PAN/PMMA nanocomposite ribbons (hot drawn to λ = 1, 3 and 5). The temperature change includes the range in which PAN nanofibers buckle within PMMA matrix (Reprinted with permission from [67]).

When the sample is heated to ~160 °C (above the glass transition temperature of the PMMA) during the thermal stabilization process, the entropic forces will drive the recoiling of the PMMA chains, leading to considerable shrinkage. Since chain alignment achieved in PMMA during hot-drawing is expected to be proportional to hot-drawing ratio, it is not surprising that the magnitude of the shrinkage is directly related to the hot-drawing ratio (compare cases of PAN/PMMA with λ=3 and 5, Figure 3). It is also interesting to note that the shrinkage profile of the PAN/PMMA films is nearly the same as that of PMMA film, suggesting that the shrinkage of the overall dimensions of the sample is driven by PMMA phase due to its much larger relative mass.

2.3.3 Carbonization

Last step of the processing is high temperature carbonization. It was carried out in a tube furnace in inert nitrogen atmosphere. The stabilized and buckled nanofibers were placed in an alumina crucible in the tube with ends of ribbons constrained by putting small alumina blocks to prevent any further shrinkage. The tube was closed air tight on both the ends with one end connected to a nitrogen tank and the other end attached to a vacuum pump. The carbonization temperature of 1400°C was used for all samples.

2.4 Characterization

2.4.1 Shape configuration

The diameter of PAN/PMMA nanofiber was measured by using FEI Quanta 600 FE-SEM with at least 10 measurements. All other dimensional parameters were measured using image processing software ImageJ with multiple measurements of each. Wavy (2D axis) and helical fibers (3D axis) were respectively characterized in terms of output parameters such as wavelength and amplitude for wavy fibers, and pitch and helix radius for helical fibers.

Morphology of CNFs (Hot drawing ratio 1): Hot drawing ratio of 1 essentially corresponds to as obtained electrospun nanoribbon with no additional stretching. The SEM images of carbon nanofibers (CNFs) revealed that the hot drawing ratio (λ) of 1, results in straight CNFs as shown in **Error! Reference source not found.**.

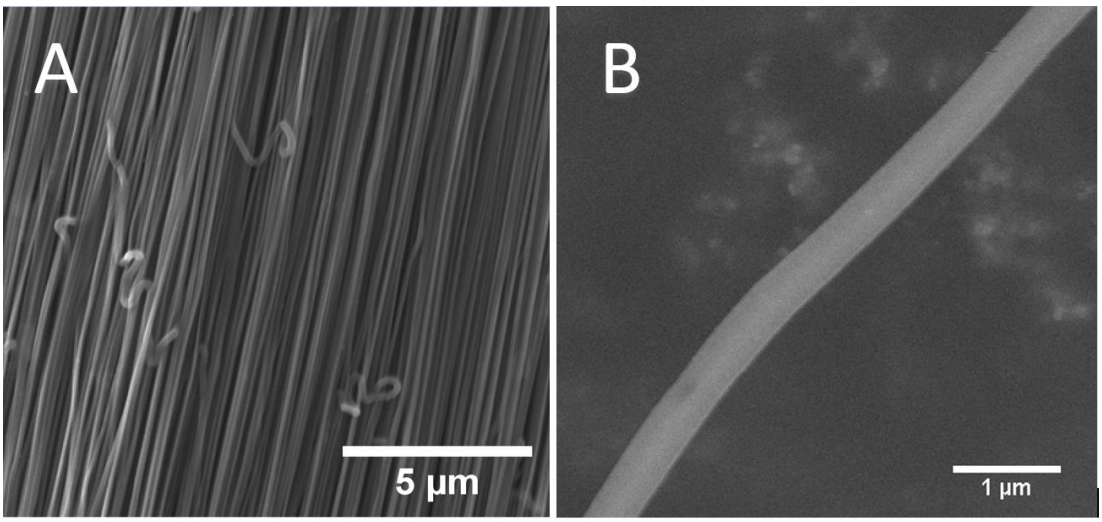

Figure 4. A) PAN nanofiber ribbons with straight aligned carbon nanofiber. B) Single carbon nanofiber (Adapted with permission from [67]).

Morphology of CNFs (Hot drawing ratio 3): Applying a hot-drawing ratio of λ=3 resulted in CNFs with a wavy profile which can be assumed as planar (2D) sinusoidal curves. In some cases, the sinusoidal fibers have shown out of plane bents, as observed in SEM images (e.g., Figure 5A). However, the in-plane bending curvature and thus the elastic energy stored in this bending mode is respectively much larger than the out-of-plane buckling curvature and the corresponding bending elastic energy.

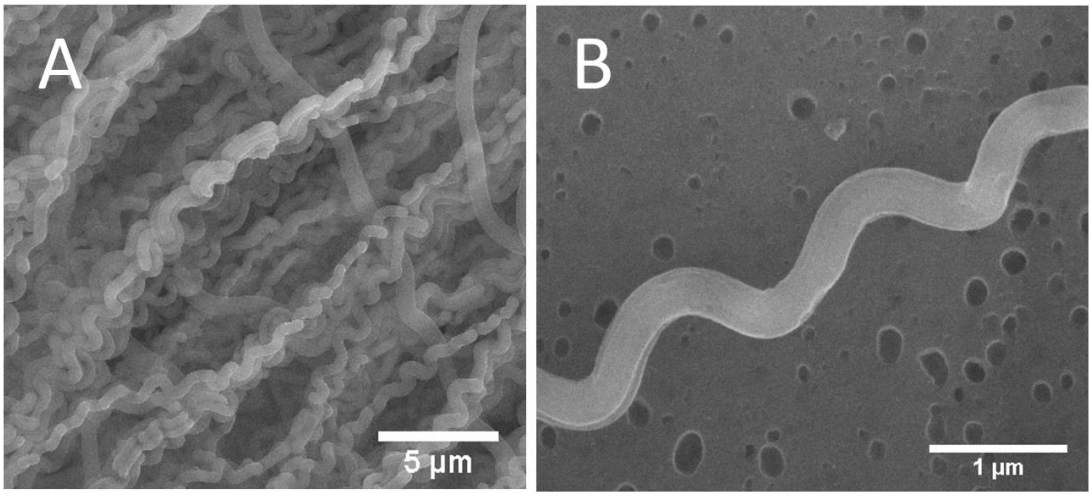

Figure 5. A) Buckled PAN sinusoidal nanofiber ribbon corresponding to λ=3. B) Single sinusoidal carbon nanofiber (Adapted with permission from [67]).

The wavelength and amplitude of wavy CNFs (mostly obtained from PAN/PMMA composite samples with $\lambda = 3$) were measured as a function of the CNF diameter from SEM images such as those shown in Figure 5B. It was observed that both wavelength and amplitude increase with fiber diameter, as shown in Figure 6.

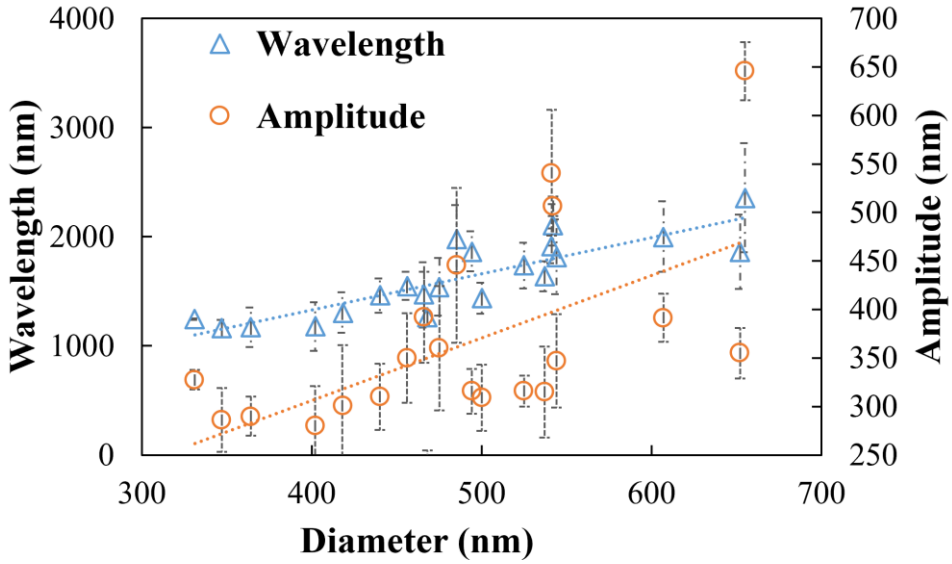

Figure 6. Change in wavelength and amplitude with respect to the fiber diameter sinusoidal fibers, which formed at hot drawing ratio 3 (Adapted with permission from [67]).

Morphology of CNFs (Hot drawing ratio 5):

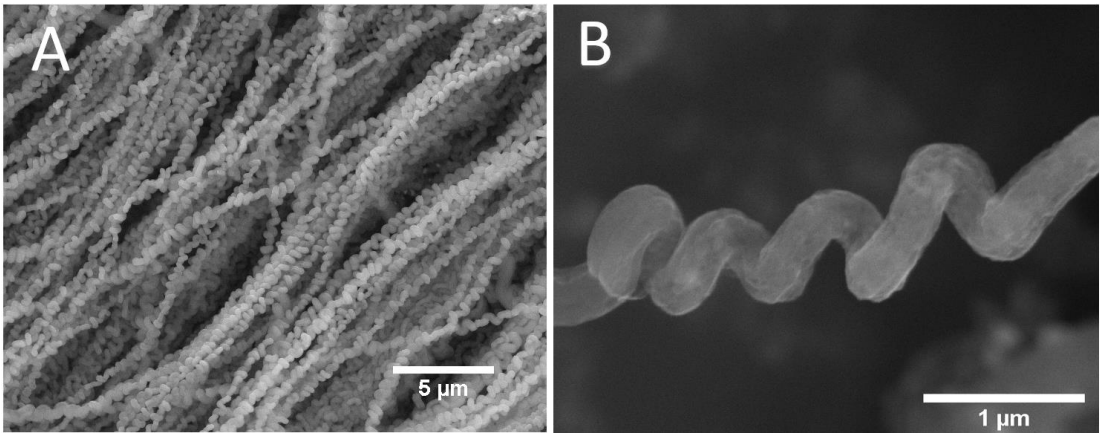

Figure 7**.** A) Buckled PAN helical nanofiber ribbon corresponding to λ=5. B) Single helical carbon nanofiber (Adapted with permission from [67]).

Whereas samples made with λ=5 exhibited a helical shape. Similarly, SEM images of helical fibers (mostly obtained from PAN/PMMA composite samples with λ = 5), such as those in

Figure 7, revealed a nearly linear increase in pitch and helix radius with fiber diameter, as shown in Figure 8.

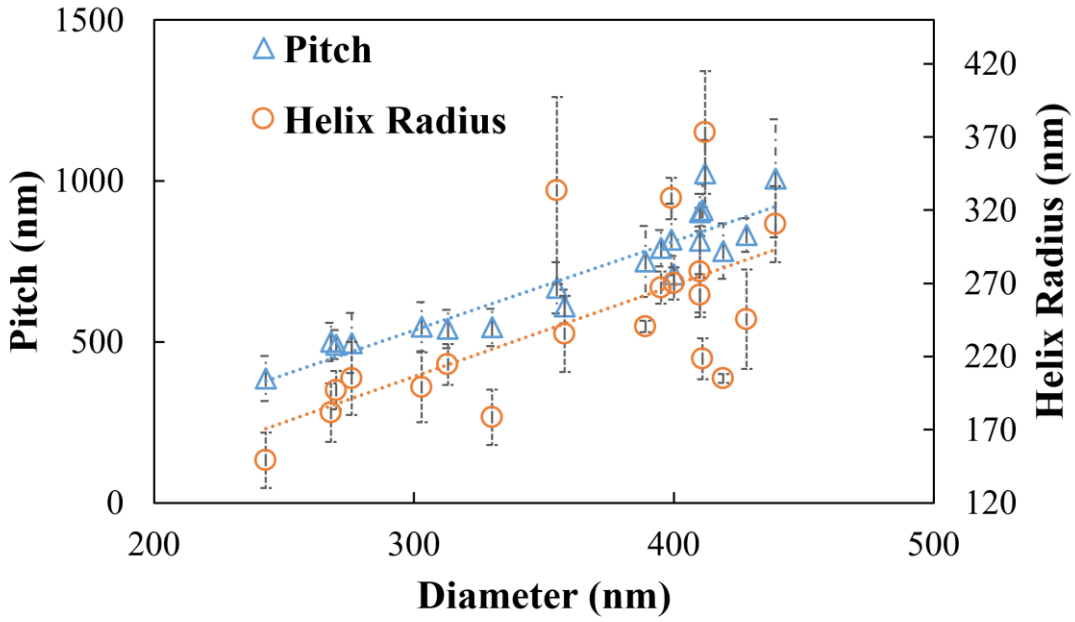

Figure 8. Change in pitch and helix radius with respect to the fiber diameter for helical fibers, which formed at hot drawing ratio 5 (Adapted with permission from [67]).

2.4.2 Surface morphology of nanosprings

As shown in Figure 9, the surface of the straight and wavy CNFs are more or less smooth, but the surface morphology of helical fibers exhibits wrinkles. The abundance of this surface morphology only in helical fibers suggests that the wrinkles form as a result of this extreme deformation.

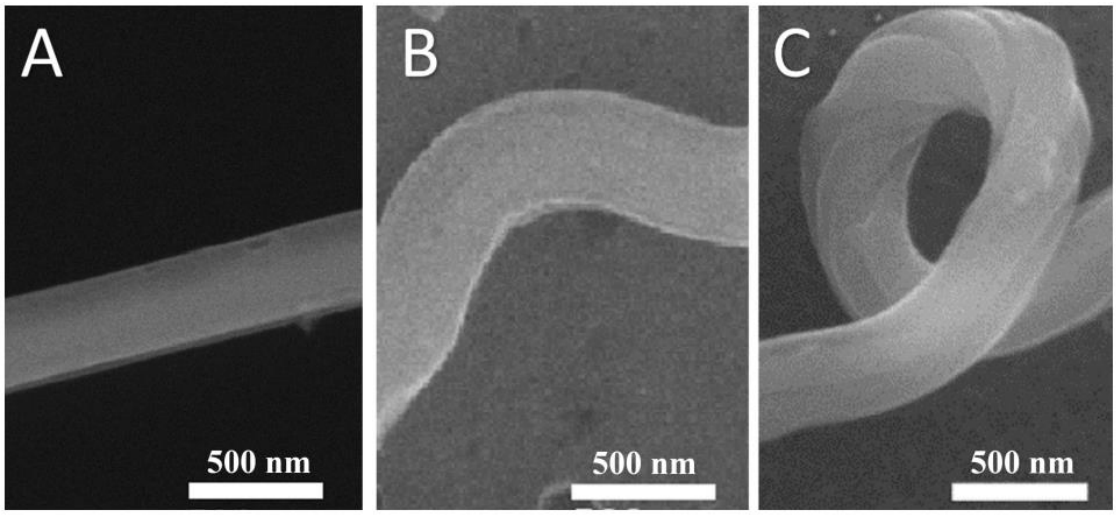

Figure 9. Surface morphology of A) straight fiber with smooth surface B) sinusoidal fiber with smooth surface, C) helical fiber with visible surface wrinkling (Reprinted with permission from [67]).

These surface features can be compared to the deformed shape of a long and thin cylindrical rod subjected to pure torsion (Torque applied parallel to the axis of the cylinder). The torque is known to provoke a twisting instability, evolving from an initial kink to a knot, and if this deformation is hindered, for example, by a surrounding matrix, wrinkles (surface instability) occur on the surface at a given critical angle of torsion [63,

64]. All of these conditions are present when the helical CNFs form, that is, torsion is inherently induced when a helix is compressed axially, and PMMA matrix applies constraint resulting in the instability on the soft surface of PAN nanofibers as they buckle.

2.4.3 Dynamic Mechanical Analysis (DMA)

As the modulus values of both polyacrylonitrile (PAN) and poly (methyl methacrylate) (PMMA) change with hot drawing & temperature. We carried out detailed dynamic mechanical analysis with temperature sweep from 30-160°C of pure PAN and PMMA films (hot drawn to λ = 1, 3 & 5) to obtain exact modulus values and moduli ratio.

DMA of polyacrylonitrile (PAN) films: PAN films were prepared by solvent casting 10 % PMMA/DMF solution in a petri dish and dried in vacuum oven at 40°C for 12 hours. Polyacrylonitrile (PAN) powder from Sigma Aldrich with a molecular weight of 150,000 g/mol was used. The films were hot drawn at 135°C to λ = 1, 3 & 5. DMA tests were carried out in TA instruments DMA 850 analyzer in tension mode, using sinusoidal stress with a frequency of 2 Hz and amplitude of 5 μm. The temperature was ramped from 30 to 160°C at a rate of 10°C/min. Figure 10 shows the obtained storage modulus for different hot drawing ratios with temperature.

There was a significant jump in modulus values with hot drawing ratio with modulus values at 30°C increasing from 1.5 GPa for λ=1 to 6 GPa and 14.25 GPa for λ=3 and 5 respectively. This phenomenon can be attributed to the progressive increase in crystallinity

of the semi-crystalline PAN film on hot drawing which in turn results better mechanical stiffness.

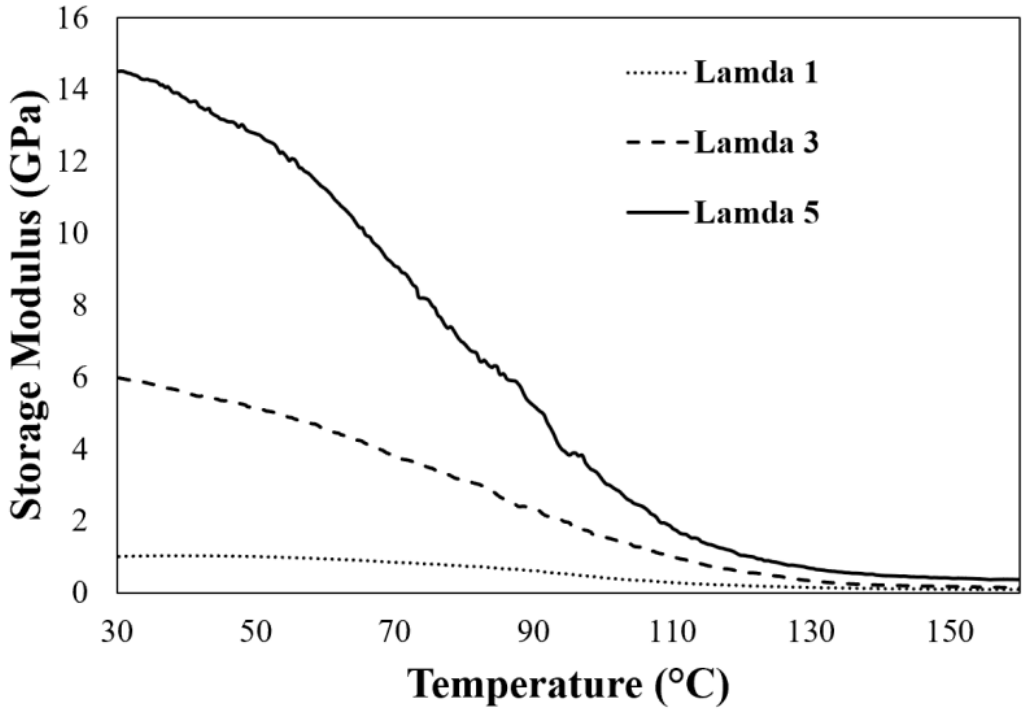

Figure 10. PAN storage modulus with temperature for different hot drawing ratio (λ = 1, 3 & 5) (Reprinted with permission from [67]).

DMA of poly methyl methacrylate (PMMA) films: PMMA films were prepared by solvent casting 10 % PMMA/DMF solution in a petri dish and dried in vacuum oven at 40°C for 12 hours. The films were hot drawn at 135°C to λ = 1, 3 & 5. DMA tests were carried out in TA instruments DMA 850 analyzer in tension mode, using sinusoidal stress with a frequency of 2 Hz and amplitude of 5 μm. The temperature was ramped from 30 to 160°C at a rate of 10°C/min. Figure 11 shows the obtained storage modulus for different hot drawing ratios with temperature.

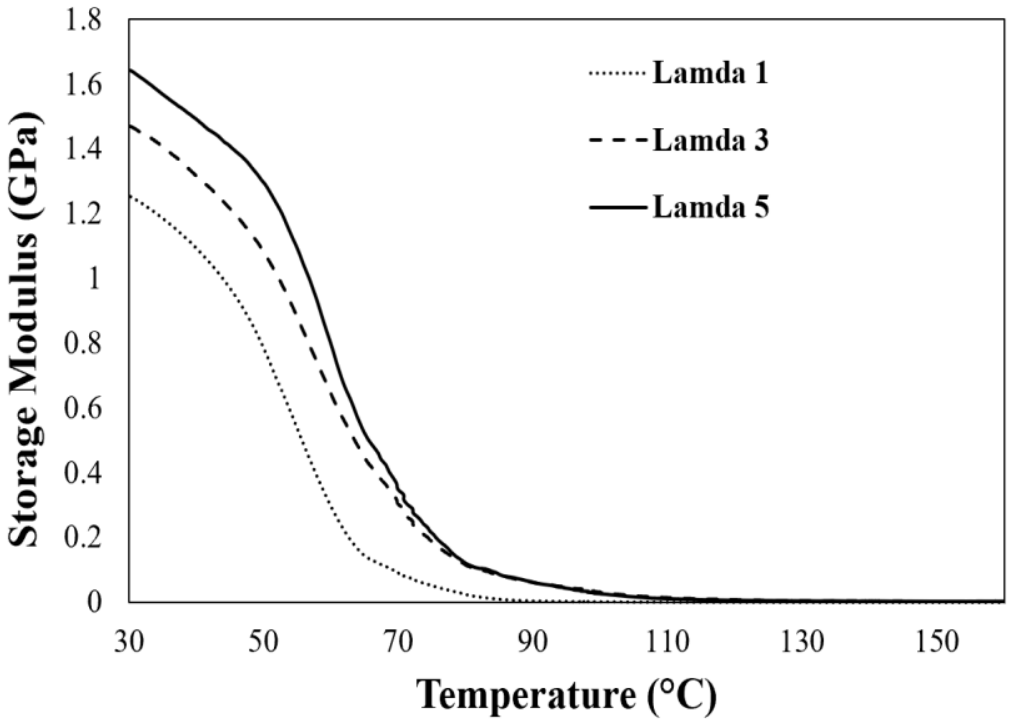

Figure 11. PMMA storage modulus with temperature for different hot drawing ratio (λ = 1, 3 & 5) (Reprinted with permission from [67]).

The relatively low increase in modulus at 30°C in case of PMMA with hot drawing can be attributed to the amorphous nature of PMMA which does not show hot drawing induced crystallization to the same extent as a semi-crystalline polymer. Additionally, at high temperature of 150° C, the difference between modulus values of different hot drawn samples is observed to be negligible, with all of the samples producing a value of ~ 2 MPa.

Ratio of PAN to PMMA Elastic Moduli as a Function of Temperature:

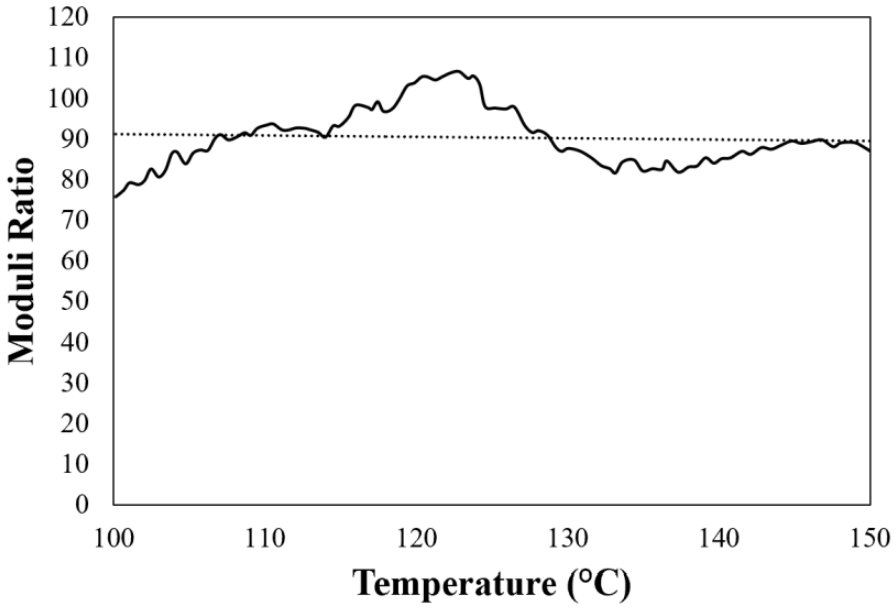

Figure 12. The ratio of moduli of PAN and PMMA for λ=3 as a function of temperature (Reprinted with permission from [67]).

As PAN fiber and PMMA matrix moduli ratio is critical to predict the buckling shape (wavy vs. helical) in the temperature range of 100-150°C, we calculated the moduli ratio for both λ=3 and 5 samples using the above DMA results. The moduli ratio for λ=3 can be assumed to be constant around 90 over the temperature range of 100-150°C as shown

in Figure 12. Similarly, for λ=5, it can also be assumed to be constant around 250 as shown in Figure 13.

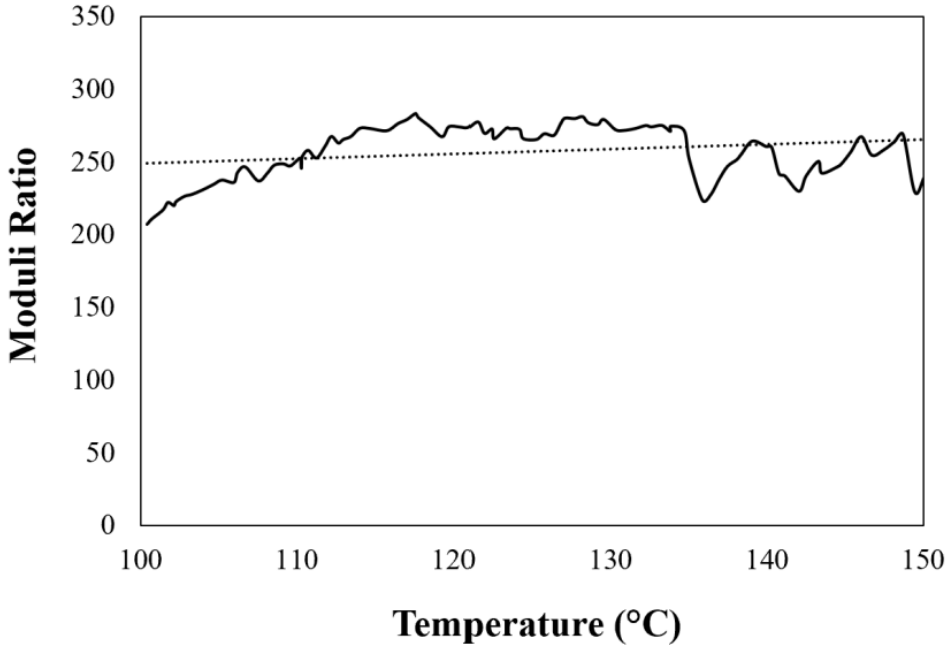

Figure 13. The ratio of moduli of PAN and PMMA for λ=5 as a function of temperature (Reprinted with permission from [67]).

2.5 Conclusion

The experiments revealed the direct correlation of hot drawing ratio to observed entropic shrinkage of PAN/PMMA nanocomposite ribbon which in turn results in buckling with a specific shape configuration. In this regard, λ =1, did not show any noticeable shrinkage while λ =3 resulted in a shrinkage of ~ 25% and buckling shape equivalent to a 2D sinusoidal shape. On the other hand, λ =5 resulted in a shrinkage of ~ 60% and a buckling profile equivalent to a 3D helical shape. The reason for shrinkage was revealed to be

mainly thermal and entropic shrinkage of PMMA matrix due to the amorphous nature which in turn provided the required compressive force to buckle the nanofibers. The input parameters of hot drawing ratio and fiber diameter were correlated to obtained structural profile of buckled fibers, in case of $\lambda=3$, both the wavelength and amplitude of sinusoidal fibers linearly increased with diameter of the fiber. Similarly, for $\lambda=5$, the helical radius and pitch linearly increased with diameter. DMA analysis validated the amorphous nature of PMMA as the modulus increase with hot drawing ratio was minimal while PAN showed a significant increase in modulus due to the hot drawing induced crystallization resultant of semi-crystalline nature.

3 MICROBUCKLING MODEL*

The shape of the wavy carbon nanofibers observed in this study resembles those of fibers subjected to buckling inside an elastic matrix [59-61]. In our study, the buckling of PAN nanofibers can be caused by the entropic shrinkage of the PMMA matrix during the thermal stabilization. Here, we present a modeling scheme based on elastic energies stored in a matrix-fiber system to capture the formation of wavy/helical fibers. The buckled shape of fibers can be explained in terms of the energy minimization principle, including the elastic energy stored in the fiber as it buckles and the energy stored in the matrix as it is pushed away by a buckling fiber. This analysis only considers the post-buckled shape of the fiber.

3.1 Background and assumptions

We thus assume that during the shrinkage of the matrix, the energy released by the recoiling of the PMMA chains will be partly stored as mechanical (elastic) energy in the fibers as they undergo buckling. The buckling will also displace the matrix laterally, storing mechanical (elastic) energy in the matrix. We further assume that the deformation of the fibers and lateral deformation of the matrix during the shrinkage is elastic, and that the wavy/helical shape of the fiber will be maintained post-buckling as fibers go through thermal stabilization (chemical crosslinking) and carbonization. The

*Portions of this chapter are reprinted or adapted with permission from [67], Sumit Khatri, Jizhe Cai and Mohammad Naraghi, "Formation of wavy carbon nanofibers and nanocoils via precursor constrained microbuckling." Journal of the Mechanics and Physics of Solids, Volume 134, 103763, 2020. Copyright [2019] by PERGAMON. Doi: https://doi.org/10.1016/j.jmps.2019.103763.

primary components

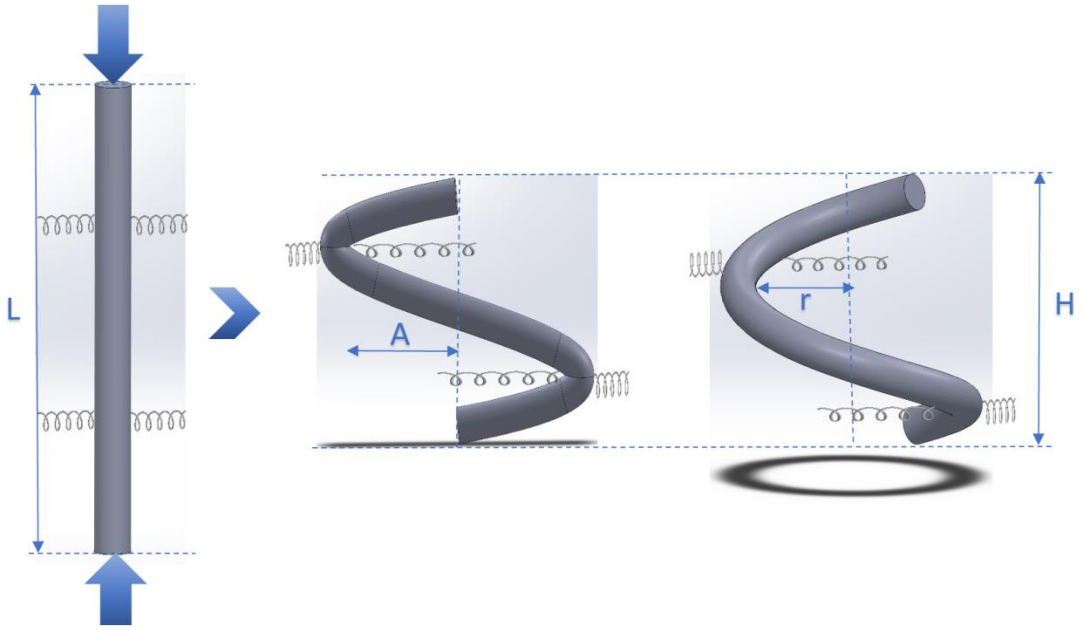

Figure 14. Straight PAN nanofiber surrounded by PMMA matrix buckled into sinusoidal and helical fiber matrix. The springs represent the equivalent elastic response of the matrix (Reprinted with permission from [67]).

of the model are shown in Figure 14.

3.2 Elastic energy stored in a system of microbuckled wavy fiber-matrix (sinusoidal)

The model contains a fiber with the initial length L which buckles into a sinusoidal shape. As a result of the buckling, the end-to-end distance of the fiber will change from L to αL, as shown in Figure 15A, where $0 < \alpha < 1$. For example, for a matrix shrinkage of 25% (engineering strain of - 25%) where the end-to-end distance of the fiber is reduced by 25%, α is 0.75. Due to the much larger mass of the matrix, it is safe to assume that the relative

change in the end-to-end distance of the fiber is equal to the shrinkage in the matrix, with the former being accommodated via microbuckling. Thus, for a given shrinkage in the matrix, a wavy fiber can deform into various mode shapes, Figure 15A. The mode shapes can be identified by a positive integer n, such that the end-to-end distance of the buckled fiber is equal to the product of n and half the wavelength of the fiber, H (Figure 14), i.e., $H = 2\alpha L/\, n.$

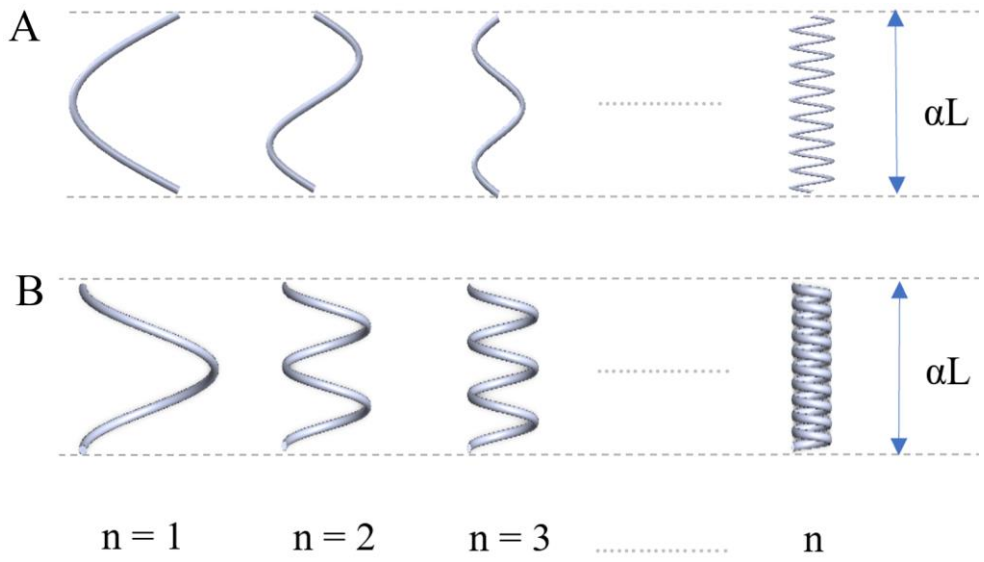

Figure 15. A) Mode shapes of sinusoidal, here, mode shape (n) is defined as n = 2αL/H where H is the wavelength in meters and B) helical buckling mode shapes, here, mode shape (n) is defined n = αL/H where H is the pitch in meters (Reprinted with permission from [67]).

The shape of a wavy fiber with amplitude A and wavelength H can be described as:

$$y = A \sin(2\pi x/H) \tag{1}$$

The strain energy stored in sinusoidal fiber can be calculated as:

$$U = \int_0^{\alpha L} \frac{M^2}{2EI}\, dx \tag{2}$$

where α is the ratio of the final to initial end-to-end distance of the fiber. In addition, the magnitude of the moment can be expressed as the radius of curvature of the buckled fiber at an arbitrary position x as,R_{sin},

$$M = -EI/R_{sin} \tag{3}$$

where R_{sin} is the radius of curvature of sine curve, to be calculated from equation (1). From (1)-(3), the strain energy in sinusoidal fiber becomes

$$U_{sin_{fib}} = \int_0^{\alpha L} \frac{\left(\left(\frac{2\pi^2 EIA}{H^2}\right) Sin^2\left(\frac{2\pi x}{H}\right)\right)}{\left(1 + \left(\frac{4\pi^2 A^2}{H^2}\right) Cos^2\left(\frac{2\pi x}{H}\right)\right)^3}\, dx \tag{4}$$

The microbuckling of the fiber is accommodated by the displacement of the matrix. The energy stored in the matrix can be estimated as follows. We represent the matrix as a combination of linear springs aligned perpendicular to the fiber axis as the matrix is assumed to behave linear elastically, shown schematically in Figure 14. The stiffness of these springs is a function of the elastic modulus of the matrix, as estimated elsewhere

[59]. Matrix displacement (y) will be captured in the model as elongation/compression in springs which stores energy in the matrix as:

$$y = \int_0^{\alpha L} \frac{1}{2} k y^2 dx \tag{5}$$

where *k* of the matrix (stiffness per unit area) is calculated based on the work of Darby [59] as,

$$k = 8\sqrt{2G_m E_m} \tag{6}$$

In equation (6), E_m and G_m are the tensile and shear moduli of the surrounding matrix respectively. Combining equations (1), (5) and (6) ultimately gives us the energy stored in the matrix for wavy nanofiber as:

$$U_{sin_{mat}} = \frac{kA^2H}{8\pi}\left(\frac{2\alpha\pi L}{H} + \frac{Sin\left(\frac{4\alpha\pi L}{H}\right)}{2}\right) \tag{7}$$

From equations (4) and (7), the total strain energy in the fiber and matrix during sinusoidal buckling can be estimated as:

$$U_{sin} = \int_0^{\alpha L} \frac{\left(\left(\frac{2\pi^2 EIA}{H^2}\right) Sin^2\left(\frac{2\pi x}{H}\right)\right)}{\left(1 + \left(\frac{4\pi^2 A^2}{H^2}\right) Cos^2\left(\frac{2\pi x}{H}\right)\right)^3} dx + \frac{kA^2H}{8\pi}\left(\frac{2\alpha\pi L}{H} + \frac{Sin\left(\frac{4\alpha\pi L}{H}\right)}{2}\right) \tag{8}$$

3.3 Elastic energy stored in a system of microbuckled wavy fiber-matrix (helical)

The energy stored in the system during the formation of the helical fibers can be calculated using a similar approach. For a given shrinkage in the matrix, a wavy fiber can deform into various mode shapes, Figure 15. The mode shapes can be identified by a positive integer *n*, such that the end-to-end distance of the buckled fiber is equal to the product of *n* and the pitch of the helical fiber (Figure 15B), $H = \alpha L/n$.

In a helical fiber, an arbitrary point on the helix has spatial coordinates of [R cos θ, R sin θ, (H/2π) θ], where θ is the radial angle ranging from 0 to 2π and *H* is the pitch of the helix for various mode shapes. The tangential direction at this point is then identified with a vector with the following components (-R sin θ, R cos θ, H/2π). The length of one turn of the helix is thus $L = 2\pi\sqrt{R^2 + H^2/(2\pi)^2}$. We take *L* as a constant (i.e., the initial length of the fiber, ignoring axial deformations of the fiber). Thus, the in-plane radius of the helix (the radius of the projection of the fiber on a plane normal to the pre-buckling fiber axis) is:

$$r = \frac{1}{2\pi}\sqrt{L^2 - H^2} \tag{9}$$

The radius of curvature, R_{hel}, is:

$$R_{hel} = \frac{r^2 + \left(\frac{H}{2\pi}\right)^2}{r} \tag{10}$$

Therefore, the bending moment in the fiber will be:

$$M = -EI/R_{hel} \tag{11}$$

Using equation (2), we can estimate the strain energy stored in fiber as:

$$U_{hel_{fib}} = \alpha EIL \Big/ 2\left(\frac{\frac{1}{4\pi^2}(L^2 - H^2) + \left(\frac{H}{2\pi}\right)^2}{\frac{1}{2\pi}\sqrt{L^2 - H^2}} \right)^2 \tag{12}$$

Here, we have neglected the effect of shear and torsion, as we expect insignificant contributions from them to the overall energy functions as explained in the section 3.7.

The energy stored in the matrix which is deformed by a helical fiber can be calculated as follows. Considering a circular helix, each point on the curve lies at a distance r from the axis, thus, the displacement function (y) of the matrix can be approximated as the radius of the helix (Equation (9)):

$$y = \frac{1}{2\pi}\sqrt{L^2 - H^2} \tag{13}$$

Hence, the energy stored in the matrix in the case of helical fiber becomes:

$$U_{hel_{mat}} = \left(\frac{1}{2} ky^2 \right) \alpha \mathrm{L} = \frac{\alpha k}{8\pi^2}(L^2 - H^2)\mathrm{L} \tag{14}$$

Combining (12) and (14), the total energy stored in helical buckling becomes:

$$U_{hel} = \alpha EIL \Big/ 2\left(\frac{\frac{1}{4\pi^2}(L^2 - H^2) + \left(\frac{H}{2\pi}\right)^2}{\frac{1}{2\pi}\sqrt{L^2 - H^2}} \right)^2 + \frac{\alpha k}{8\pi^2}(L^2 - H^2)L \qquad (15)$$

3.4 Predictions of the shape of the nanosprings

We used the model developed in section 3 to predict the shape of the wavy fibers and helical fibers and also to identify which shape (helical/wavy) is more energetically favorable. To this end, for an experimentally measured value of matrix shrinkage and mode shape, we calculated the energy stored in each form, wavy or helical fibers. For each deformed shape (wavy or helical), the energy becomes the lowest for a certain value of *n*. Lower and higher n values will result in higher stored energy in the fiber-matrix system due to respectively excessive matrix deformation and sharp bents (curvature) of the fiber. The mode shape which resulted in the lowest energy was calculated by considering various values of *n*. The minimum energy states of the two shapes were then calculated and the deformed shape and mode shape with the lowest energy was reported as the predicted prevailing shape (Equations 8 and 15). The corresponding value of *n* (representing the mode shape) was used to calculate the predicted wavelength of the wavy fibers and the pitch of the helical fibers. The results are then compared with the experiments.

3.4.1 Predictions of the shape of the helical fibers (λ=5, helical)

As an example, to predict the pitch and helix radius of a fiber buckling in helical shape for

λ=5, we started with a 400 nm thick fiber with an initial straight length of 10 cm, which is the same as the actual length of PAN-PMMA ribbon used in experiments. This ribbon reduces to the length of 4 cm after 60% shrinkage as shown in Figure 3 for λ=5. Using the helical buckling model presented in section 3.4, we plotted the energy stored in fiber (equation 12) and matrix (equation 14) as fiber buckles into a helix, starting with first mode shape (i.e. only one turn of the helix) to thousands of turns. A critical parameter to calculate the energies in fiber and matrix is their elastic moduli. As shown in Figure 3, most of the shrinkage of PMMA which leads to buckling of PAN nanofibers occurs within the temperature range of 100-150 ˚C. According to the results of DMA analysis, within this range of temperature, the ratio of the moduli of PAN to PMMA remains nearly independent of temperature, but highly dependent on drawing ratio (λ). This ratio is around 90 for λ=3 and 250 for λ=5 as shown in the Figure 12 and Figure 13 respectively.

The modulus values change with hot drawing and temperature, hence, the input values used for the model here are taken from DMA analysis for hot drawing ratio (λ) of 5 at a specific temperature of 150˚C. The elastic modulus of PAN fiber is 441 MPa and 1.8 MPa for the PMMA matrix, the Poisson's ratio for PMMA at 150 ˚C (much higher than PMMA glass transition temperature) is taken as 0.5 referenced from the book of Bicerano [65], and the shear modulus is obtained using the isotropic material behavior. The results are plotted in Figure 16A. As shown in the plot, the minimum energy state is reached when the helix has a mode shape of 25000, resulting in minimum energy of 0.17 μJ.

We then proceeded by calculating the minimum energy that will be stored in a wavy buckling mode when subjected to a matrix shrinkage of 60%. In this case, the minimum stored energy will happen for mode shape of 50000, resulting in minimum energy of 3.5 μJ. This value is much higher than the energy stored in the helical buckling, leading to the prediction that at $\lambda=5$ it is the helical fiber shape that prevails at the lowest energy state.

Dividing the experimental buckled length of 4 cm with these number of turns of the minimum energy state of the helical fiber gives us the value of pitch (H) to be 1.6 μm which is close to the experimentally measured value of 0.9 μm, for the 400 nm thick fiber (Figure 8). Using equation 14, the radius of curvature comes out to be 590 nm which of the same order as the experimentally observed value of around 280 nm. The difference between the experimental values and the predicted from the model can be attributed to the assumptions of linear behavior and a large range of diameter distribution of fibers in the PAN ribbon as well as imperfect alignment.

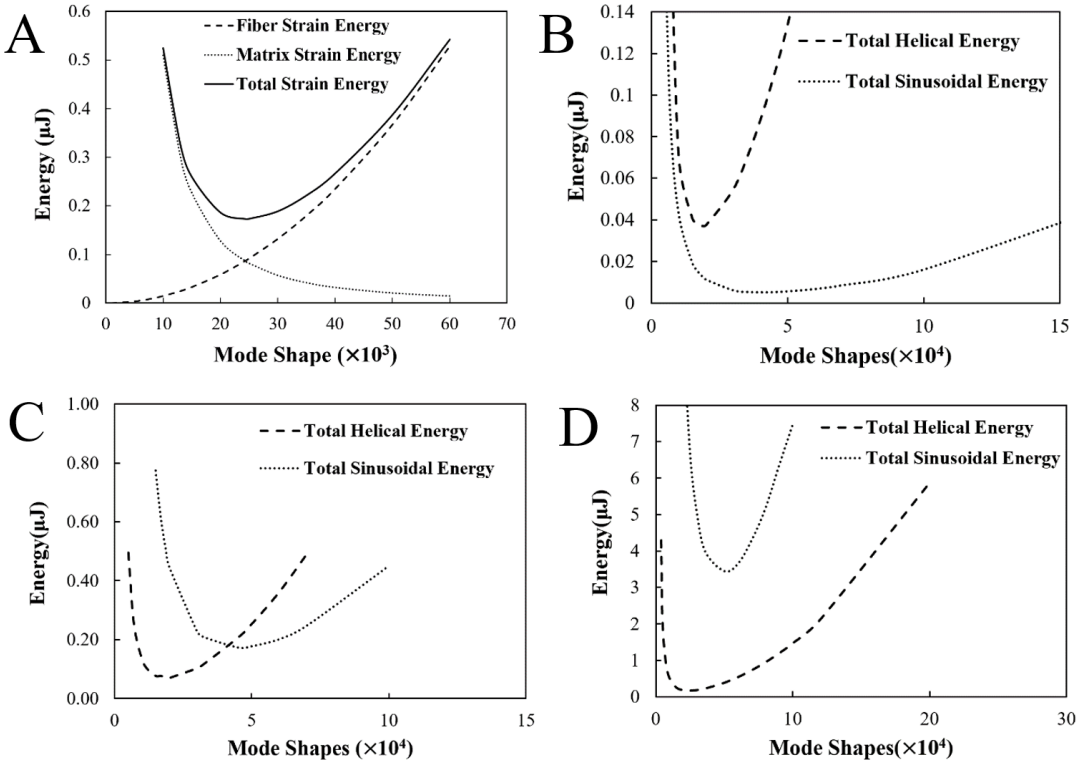

Figure 16. A) Strain energy stored in fiber and matrix in helical buckling of a 400 nm diameter fiber with initial straight length of 10 cm, surrounded by a matrix with $E_f/E_m = 250$ for $\lambda=5$ at 150° C, showcasing the mode shape with minimum energy for pitch and helix radius prediction. Here, mode shape (n) is defined as n = 0.04/H where H is the pitch in meters. B) Total energy comparisons between sinusoidal and helical buckling for the case of 10 % shrinkage revealing the energetically favorable sinusoidal buckling mode C) For 25% shrinkage ($\lambda=3$), revealing that both buckling modes are energetically favorable as the minimum energy state are of same order D) For 60% shrinkage ($\lambda=5$), revealing the energetically favorable helical buckling mode. In all cases, mode shape (n) for helical buckling is defined as n = 0.04/H where H is the pitch in meters and mode shape (n) for sinusoidal buckling is defined as n = 0.09/H where H is the wavelength in meters (Reprinted with permission from [67]).

3.4.2 Predictions of the shape of the wavy fibers (λ=3, sinusoidal)

The modulus values change with hot drawing & temperature, hence, the input values for hot drawing ratio (λ) of 5 are different than λ=3 at same temperature of 150˚C. The elastic modulus of PAN fiber is 183 MPa and 2.1 MPa for the PMMA matrix, the Poisson's ratio for PMMA at 150 ˚C is taken as 0.5 as earlier. The length of straight fiber (L) is taken as 6 cm which was the actual length of PAN/PMMA ribbon after stretching to hot drawing ratio of λ=3 which in turn shrunk to 4.5 cm i.e. 25% shrinkage.

The results are plotted in Figure 17, from the plot, the minimum energy state is reached when the sinusoidal curve has 22500 full wavelengths (or mode shape of 45000), dividing the experimental buckled length of 4.5 cm with 22500 gives us the value of wavelength (H) to be 2 μm which is close to 1.2 μm, the actual value of wavelength of a 400 nm fiber buckled to sinusoidal shape as observed in experiments. Amplitude can be obtained from the arc length (L) & wavelength (H) to be 740 nm which of the same order as actual value of 280 nm.

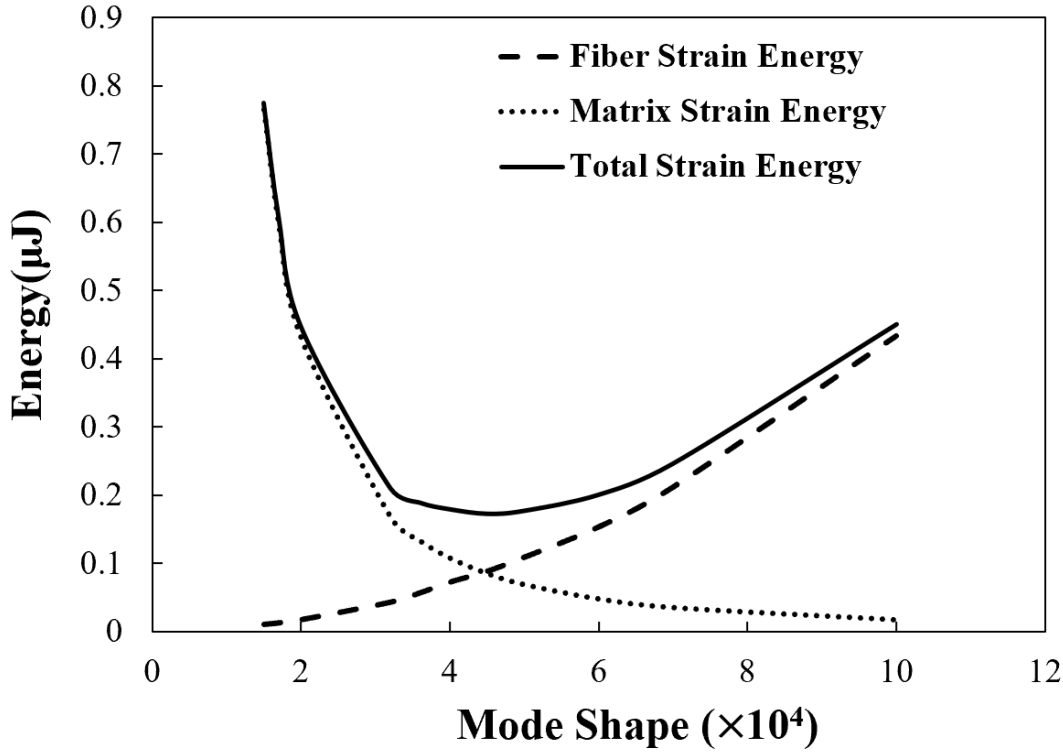

Figure 17. Strain energy stored in fiber & matrix in sinusoidal buckling of a 400 nm diameter fiber with initial straight length of 6 cm, surrounded by a matrix with Ef/Em = 90 for λ=3 at 150° C, showcasing the mode shape with minimum energy for wavelength and amplitude prediction. Here, mode shape (n) is defined as n = 0.09 /H where H is the wavelength in meters. (Adapted with permission from [67]).

3.5 Transition from wavy to helical CNFs, a comparison with theory

The model can also explain the transition from one shape to another by increasing the value of matrix shrinkage. To this end, we used the buckling models to plot the total energy stored in sinusoidal buckling (equation 8) and helical buckling (equation 15) as a function of the mode shape to compare the minima of energies stored in the fiber matrix system of the buckled fiber for the cases of 10%, 25% (λ=3) and 60% (λ=5) shrinkage. We took the

fiber diameter to be 400 nm and initial length of the fiber, *L*, to be 6cm. Given the periodicity in the deformation, this does not limit the scope of the applicability of these results. For 60% shrinkage, the elastic modulus of PAN fiber at 150°C is 441 MPa and 1.8 MPa for the PMMA matrix. For 25% shrinkage, the elastic modulus of PAN fiber at 150°C is 183 MPa and 2.1 MPa for the PMMA matrix. All these values were sourced from the DMA analysis. The Poisson's ratio for PMMA at 150°C is taken as 0.5. The case of 10% was added to better illustrate the trends. However, for the 10% matrix shrinkage, the elastic modulus values were not tested directly and estimated via a polynomial interpolation using DMA data for λ=1 (no shrinkage), λ=3 (25% shrinkage) and λ=5 (60% shrinkage). As shown in Figure 16, in the case of 10% shrinkage (Figure 16B), sinusoidal shape is energetically more favorable than the helical case but as we move to 25% shrinkage (Figure 16C) both the buckling modes are more or less equally favorable and at 60% shrinkage (Figure 16D), helical mode is clearly more favorable.

Building on the results of Figure 16, we plotted the minimum energies of both the sinusoidal and helical buckling modes for a range of shrinkage from 10% to 60% with appropriate scaling of material properties based on DMA data. The results are plotted in Figure 18 for a fiber with a diameter of 400 nm. The plot presents the progression of the buckling and the total mechanical energy stored in the PAN-PMMA system as a function of the shrinkage of a buckling fiber. Based on Figure 18, it is clear that for small shrinkage value, the in-plane sinusoidal configuration is the lower energy deformation compared to a helical fiber. However, as the fiber gets more and more compressed (i.e., reducing the

wavelength/pitch), there comes a transition point where helical shape becomes energetically more favorable (For the specific conditions listed in Figure 18, this value obtained is 20% shrinkage).

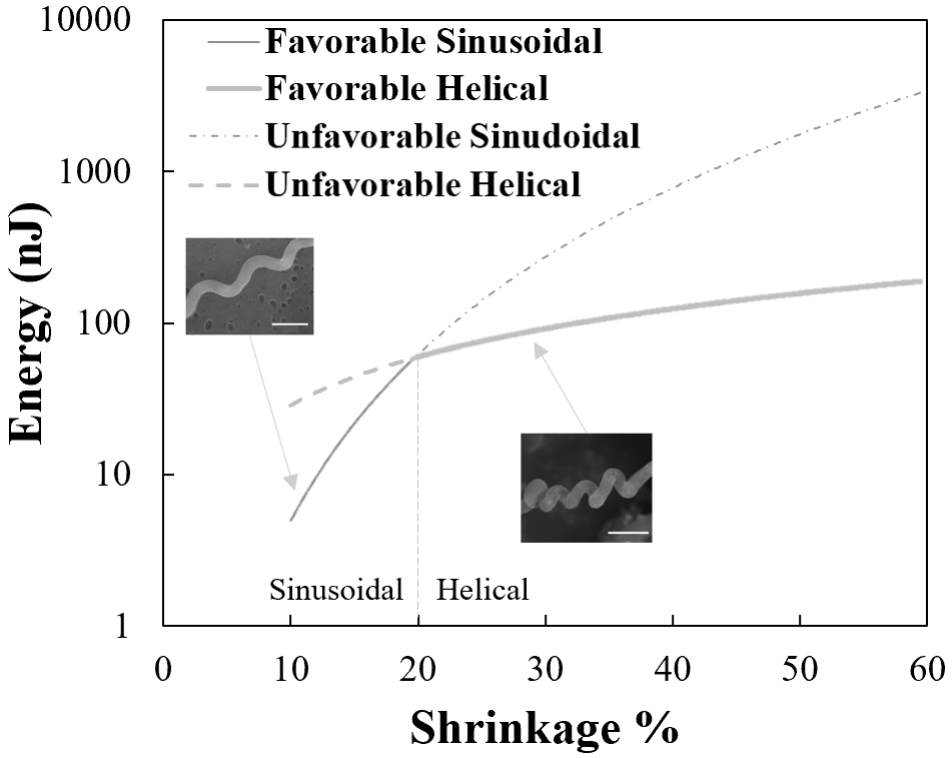

Figure 18. Total strain energy stored in case of sinusoidal and helical buckling for mode shape with minimum energy vs shrinkage of a 400 nm fiber of initial length 6 cm, showcasing the transition from sinusoidal to helical shape based on minimization of energy as shrinkage increases from 10% to 60%. (All scale bars are 1μm) (Reprinted with permission from [67]).

Qualitatively, the model prediction is in line with our experimental observation that the wavy fibers form at lower hot-drawing ratios (which correspond to lower shrinkages during stabilization).

According to our experimental observation, for low hot drawing ratio (λ) of 3 which corresponds to 25% shrinkage, we get mainly sinusoidal fibers but as we go to hot drawing ratio (λ) of 5 which corresponds to 60% shrinkage, mainly helical CNFs form as predicted from the model in Figure 18.

3.6 Effect of shear and torsion

To take care of direct shear and curvature effect in helical buckling, Wahl's factor was employed in the bending moment:

$$K_w = (4C - 1/4C - 4) + (0.615/C) \quad (16)$$

Where C is the spring index defined as: $C = D/d$

D = coil diameter, d = fiber diameter

Considering Wahl's factor did not affect the total energy stored much, so, the contribution of shear and curvature effect was neglected in the calculation.

In the case of torsion, even if we take a very high twist of 2 π, then:

Energy due to Torsion,

$$U = \int_0^L \frac{T^2}{2GJ}\,\mathrm{dx} \quad (17)$$

where T = torque, G = shear modulus and J = polar moment of inertia

$$T = \phi GJ/L \quad (18)$$

where ϕ = angle of twist, the value of G is taken is equal to young's modulus of PAN (a gross overestimation just for the check) which is 441 MPa as observed in DMA analysis at 150° C for a fiber of 400 nm diameter and length of 10 cm as is the case with λ=5. From

equation (17) and (18), we plotted energy stored in fiber due to torsion with increasing angle of twist. Energy due to torsion is negligible as compared to the total energy in helical fiber as can be inferred from Figure 16 and Figure 19. Hence, it is deduced that most of the strain energy comes due to bending with the effect of shear and torsion being negligible.

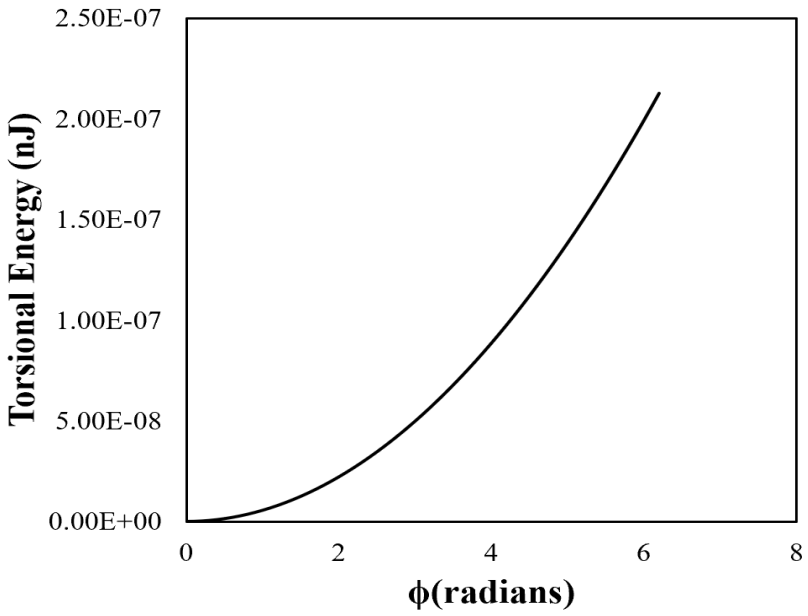

Figure 19. Torsional energy for 400 nm PAN fiber hot drawn to λ=5 with angle of twist (Reprinted with permission from [67]).

3.7 Conclusion

Here we have presented a novel method to produce wavy and helical carbon nanofibers (CNFs). The waviness/helicity of CNFs was achieved by subjecting the precursor PAN nanofibers to constraint buckling inside a matrix of PMMA. The shrinkage in PMMA was

induced by triggering entropic forces, while the formation of crystals in PAN nanofibers had significantly limited their ability to shrink in response to entropic forces. As a result, PAN nanofibers buckled in-plane or out-of-plane, depending on the magnitude of the shrinkage of the matrix. It was observed that the wavelength (pitch) and amplitude (helix radius) of the sinusoidal and helical fibers are directly proportional to the fiber diameter. The pitch and radius in case of helical fibers and wavelength and amplitude in case of sinusoidal fibers were predicted using minimization of strain energy stored in fiber-matrix system. The results agreed well with the experiments. The transformation of wavy fibers from sinusoidal to the helical shape by increasing the shrinkage as observed in experiments was quantitatively explained by considering the elastic energy stored in the fiber-matrix system during the thermal shrinkage.

4 EFFECT OF GEOMETRIC & MATRIAL NON-LINEARITY

The microbuckling model presented in the previous model is based on Euler Bernoulli beam theory with linearly elastic material which neglects the contribution of the plasticity and shear strain. These are reliable assumption for small strain values (~1-5% strain). However, the strain values for the buckled fiber in this study can reach as high as 25% at the peak of curvature in sinusoidal fiber which requires us to consider material and geometrical nonlinearities such as plasticity and large deformations. The beauty of the linear elastic model is that analytical equations could be derived to compare the experiments and the model. As discussed in the previous chapter, the results had satisfactory comparison with the experiments due to the limited volume of the material which experiences large deformations. Despite that some of the discrepancies observed between linear elastic model and experiments may be eliminated by considering such nonlinearities.

In this chapter, we have made the first attempts to consider the effect of plasticity and large deformations. The plasticity effect considered in this chapter is constrained to only the fiber deformation. In case of matrix, we have assumed that it is deforming as an infinite half space, and as such it remains in the elastic regime of deformation. So, these non-linear contributions cannot be analysed analytically; thus, numerical finite element method (FEM) is employed in this chapter.

4.1 Overview of the Modeling Approach

The identification of the most energetically favourable buckling mode of the fibers when subjected to matrix contraction was carried out by considering various mode shapes as discussed in Figure 15 in previous chapter. For various mode shapes, the energy stored in the fiber (considering elasto-plastic behaviour and large deformation) as well as energy stored in the matrix (elastic behaviour) for a given matrix contraction was calculated. The total energy in the system was then calculated as the sum of the energies stored in each constituent and was plotted as a function of the mode shape. The minimum energy mode shape was then reported as the most stable configuration and as the emerging one.

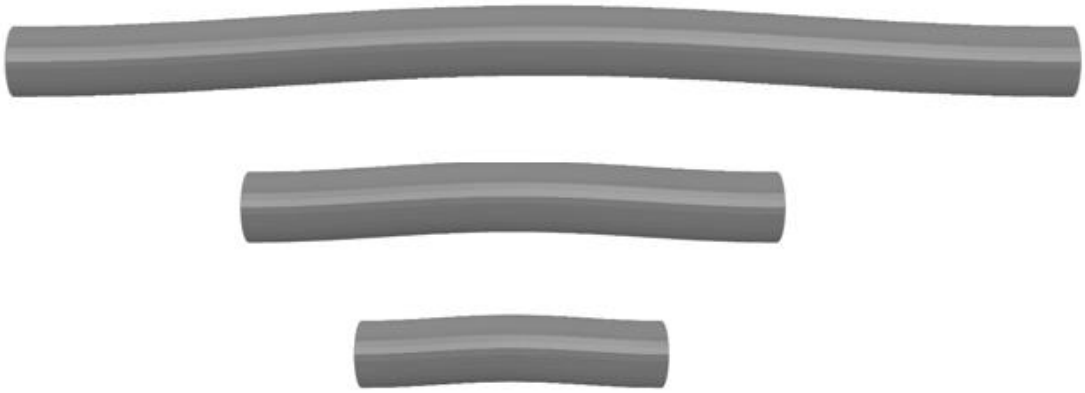

Figure 20. FEM models of 400 nm diameter PAN fibers with slight initial curvature (Initial wavelength/amplitude (L/A) =100), top to bottom, 6 μm, 3 μm and 1.8 μm.

To simulate the bending of a fiber into a sinusoidal conformation, a minimal initial fiber waviness was required so that the fiber will bend as a result of axial contraction instead of

undergoing compressive deformation predominantly. From an experimental standpoint, the initial waviness reflects the misalignment of the fibers and imperfections in the experiment. The initial waviness was defined as the ratio of the wavelength to the amplitude of the fiber with its centreline on a sinusoidal curve.

From FEM analysis, we realized that for very small waviness (Initial wavelength/amplitude ratio > 500), the initial waviness affects the bending profile significantly, as internal moments are not high enough to bend the fiber and instead fiber compresses predominantly without bending. As a result, a minimal initial curvature with initial wavelength to amplitude ratio (L/A) of 100 was employed for all models (

Figure **20**) to make sure that the fiber bends. However, it is important to note that our models revealed that the even doubling the initial waviness beyond the minimum threshold has a secondary effect on the internal energy stored in fiber subsequent to matrix shrinkage.

To obtain a mode shape with minimum strain energy pertaining to 25% shrinkage observed in λ=3, 12 models with different initial length from 8 μm to 1 μm were modelled using TexGen software. The elastic analysis presented in the previous chapter guided us in deciding which mode shapes to choose.

Figure 20 shows some of the models used for the simulation. The fiber diameter was 400 nm within the range of experiments. The boundary conditions were as follows: one end of

the fiber was fixed and a compressive displacement (equivalent to a 25% linear shrinkage) was applied at the other end.

Fully integrated C3D8 brick elements with hybrid formulation were utilized with the mesh size of 0.04 μm to account for large deformations observed in simulation. Figure 21 shows the general meshing scheme in one of the models.

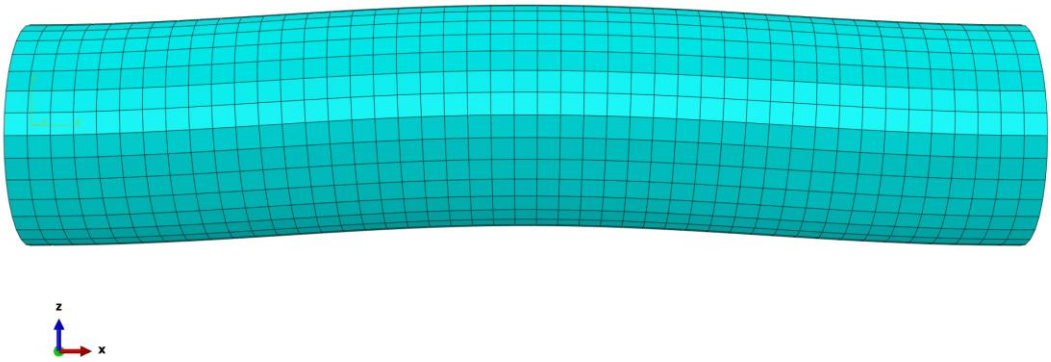

Figure 21. FEM model for a 400 nm diameter fiber with 1.8 μm initial length meshed with fully integrated C3D8 brick elements.

4.2 Material Properties

The PAN fiber is supposed to be isotropic material with the elastic modulus of 183 MPA at 150° C obtained from DMA analysis and a Poisson's ratio of 0.4. Due to the non-availability of plastic behaviour of PAN nanofibers at exact condition of stretch ratio (λ) = 3 at a temperature of 150˚C (required in our analysis to replicate the experiment), we have relied on the literature to approximate the expected plastic behaviour of PAN.

Since PAN is a semi-crystalline polymer, the stress-strain data of another semi-crystalline material, Polyether ether ketone (PEEK) in comparable conditions [66] is used as the basis to arrive at the plastic data for PAN nanofiber. Table 1 shows the factors used to compare the material response of both materials. Data available of PEEK has similar crystallinity (41%) [66] to the PAN fibers at stretch ratio (λ) = 3 (~45%) [57] and the compressive true stress-strain response data at a temperature of 200°C is used as it is around 50°C higher the than the glass transition temperature of PEEK, similar to the condition of 150°C for PAN (~50° C higher than the glass transition temperature).

Material	Behaviour	Crystallinity	T_g	Testing Temp.
PEEK	Semi-crystalline	41%	143	200
PAN	Semi-crystalline	45%	95	150

Table 1. Parameters taken in to account for selecting PEEK material response to extrapolate expected PAN stress-strain response (Adapted from [57] [66]).

The stress-strain data for PEEK at 200°C is scaled and extrapolated into PAN stress-strain data at 150°C using the available modulus value of PAN of 183 MPa and equivalent modulus value of PEEK as the reference with plastic strain response assumed to be same for both materials due to similar crystallinity and equivalent temperatures. The equivalent stress-strain approximation obtained for PAN at 150°C is shown in Figure 22.

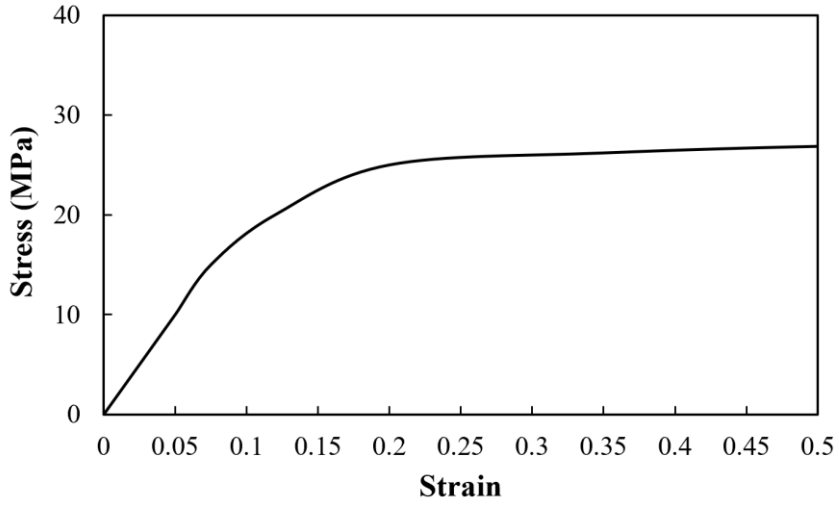

Figure 22. Stress-strain data used for PAN fiber elasto-plastic model at 150°C.

4.3 Results and Discussion

The FEM analysis was carried out using the model and material properties discussed in the previous sections. The average bending stress obtained in buckled fibers is found to be at least 4 orders higher than the average shear stresses which validated the earlier assumption (made in chapter 3) of the negligible contribution of shear stresses compared to the bending stress.

Figure 23. From left to right, buckled 400 nm diameter fiber after 25% shrinkage with wavelength 4.5 μm (initial length = 6 μm), 2.25 μm (initial length = 3 μm), 1.38 μm (initial length = 1.8 μm)

The strain energy stored in a single sinusoidal wavelength is obtained using *ELSE output parameter and multiplied by half of the mode shape number to get the overall energy stored in the 4.5 cm long buckled fiber for case of λ=3. The buckled profile generated (

Figure **23**) is used to calculate the amplitudes for respective mode shapes. As the matrix deformation is supposed to be largely elastic, the strain energy stored in the matrix is obtained by using the microbuckling model equation (7) with input parameters of wavelengths and corresponding amplitudes taken from FEM results. Figure 25 shows the plot of strain energy stored in the fiber, the matrix and the fiber-matrix system with the mode shape.

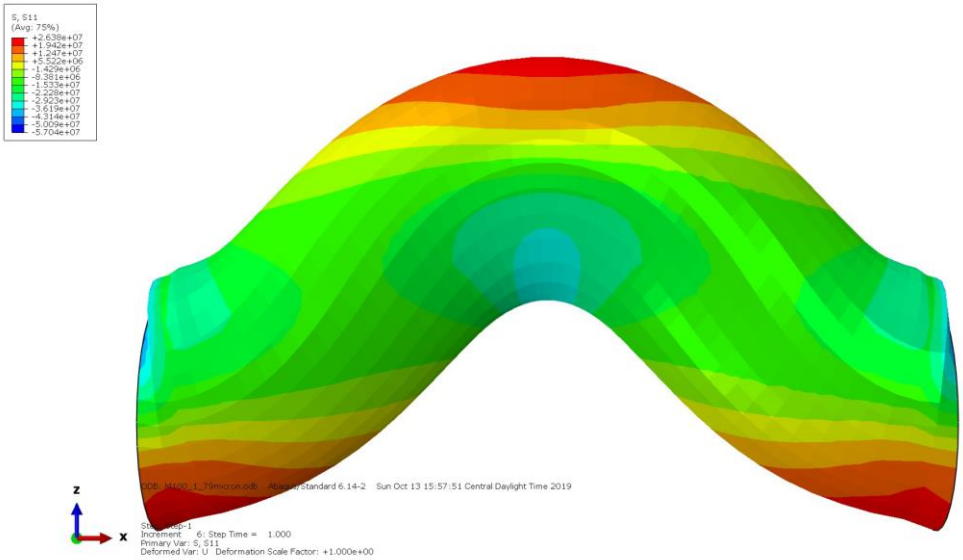

Figure 24. Bending stress in the buckled 400 nm diameter PAN fiber with wavelength of 1.8 μm.

The mode shape corresponding to the minimization of strain energy stored in the fiber-matrix system is 90000, which corresponds to a wavelength of 1 μm and an amplitude of 105 nm, which is quite close to the experimentally observed values of wavelength of 1.2 μm and amplitude of 280 nm for a fiber of 400 nm diameter.

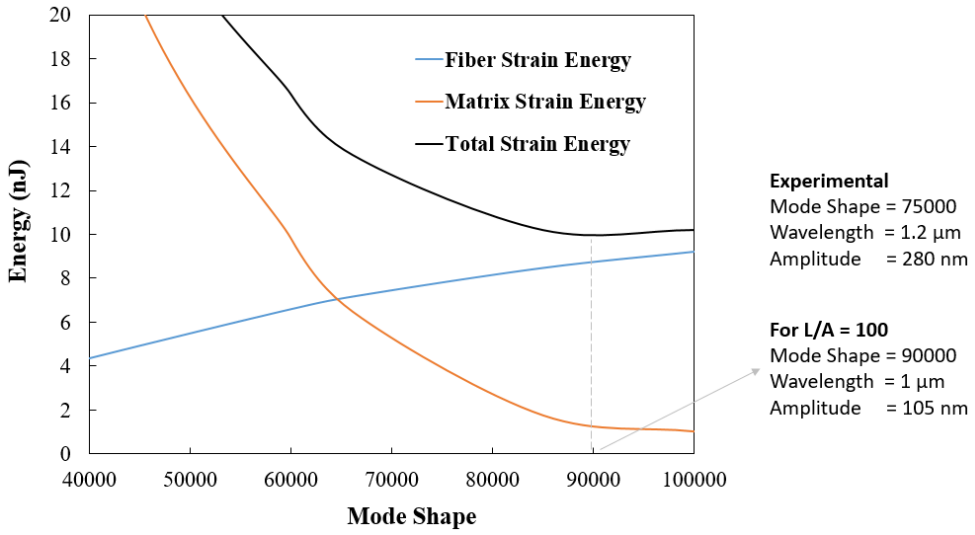

Figure 25. Strain energy stored in a 400nm fiber buckled in to a sinusoidal configuration after 25% shrinkage and the matrix as well as total energy stored in the system with respect to the mode shape. The minimum of total strain energy is reached at the mode shape (n) of 90000. Here, mode shape (n) is defined as n = 0.09/H where H is the wavelength in meters.

4.4 Conclusion

The motive of this FEM analysis was to check and validate the assumptions of negligible contribution of shear stress and try to improve on the predictions of linear elastic microbuckling model by inclusion of plasticity. FEM results validated the assumption of negligible contribution of shear stresses were at least 4 orders lower than the bending stress. Additionally, inclusion of plasticity, by using an elasto-plastic model derived from literature, the discrepancy in experimental results and the microbuckling model have been reduced to a large extent in terms of prediction of wavelength and to a lower extent in terms of predicted amplitude. The observed large error in amplitude can be attributed to

the sensitivity of the initial model curvature to the observed deformed amplitude. Moreover, the elasto-plastic data derived from a different semi-crystalline material although similar in overall response, is bound to be differ in terms of details of the stress-strain curve which directly influenced the energy stored in the fiber and underlying prediction of shape configuration. The energy lost in plastic dissipation is observed to be significant, especially at higher mode shapes with large curvatures.

5 SUMMARY & FUTURE DIRECTIONS

5.1 Conclusions

Here we have presented a novel method to produce wavy and helical carbon nanofibers (CNFs). The waviness/helicity of CNFs was achieved by subjecting the precursor PAN nanofibers to constraint buckling inside a matrix of PMMA. The shrinkage in PMMA was induced by triggering entropic forces, while the formation of crystals in PAN nanofibers had significantly limited their ability to shrink in response to entropic forces. As a result, PAN nanofibers buckled in-plane or out-of-plane, depending on the magnitude of the shrinkage of the matrix. It was observed that the wavelength (pitch) and amplitude (helix radius) of the sinusoidal and helical fibers are directly proportional to the fiber diameter. The pitch and radius in case of helical fibers and wavelength and amplitude in case of sinusoidal fibers were predicted using minimization of strain energy stored in fiber-matrix system by assuming linear elastic behavior. The transformation of wavy fibers from sinusoidal to the helical shape by increasing the shrinkage as observed in experiments was quantitatively explained by considering the elastic energy stored in the fiber-matrix system during the thermal shrinkage. The results agreed well with the experiments in terms of order of prediction which is acceptable in view of assumption of linear elastic behavior in a large deformation scenario, especially at higher mode shapes.

Finite element analysis was carried out to account for the inherent underlying non-linearities in terms of high strain and material plasticity as well as assumptions of negligible contribution of shear stresses in sinusoidal buckling. FEM results validated the assumption of negligible shear stress contribution and improved the prediction of experimentally observed shape configuration to a large extent, especially in terms of wavelength where the experimentally observed wavelength of 1.2 μm was predicted by FEM to be 1 μm in contrast to 2 μm predicted by linear elastic microbuckling model.

Overall, this study analysed the processing and structure relationships between the input parameters like fiber diameter and hot drawing ratio with output parameters like wavelength and amplitude in case of the fibers buckled in sinusoidal shape while helix radius and pitch in the case of helical buckling. Substantial importance was given to understand the underlying mechanics behind the buckling of fibers and the experimental observations were successfully predicted by developing a mechanics based linear elastic microbuckling model and later improved on by accounting for geometric and material non-linearities by employing FEM analysis.

5.2 Future directions

To complete the triad of processing-structure-property relationships, the next step will be to do mechanical & electrical characterization of individual nanosprings using microelectromechanical (MEMS) devices to validate the potential of these novel nanostructures as a multifunctional material.

Additionally, the microbuckling model overpredicted the shape configuration while the FEM analysis underpredicted the expected results, although to a smaller extent. The accuracy of FEM analysis can be improved by utilizing the exact experimental stress-strain curve for PAN at different hot drawing ratio which potentially will lead towards convergence with observed experimental values.

Moreover, this study relied on the observation of the final buckled shape configuration due to the inherent size & scale limitations imposed by nanoscale to do in-situ observations. The theory developed in the microbuckling model will hold good at all scales as it is based on mechanics, in fact, this analysis will arguably be more correct at scales larger than nano as at the nanoscale the polymer free volume and chain interactions affect the results and even the assumption of continuum can be challenged. To do an in-situ observation to understand the underlying physics of this buckling phenomenon, a micro or larger scale analysis can be carried out by buckling PAN microfibers inside a transparent amorphous polymer matrix to study the evolution of buckling.

REFERENCES

[1] A. M. Wahl, *Mechanical Springs*, First ed. Cleveland, Ohio: Penton Publishing Company, 1944.

[2] X. Chen *et al.*, "Mechanics of a Carbon Nanocoil," *Nano Letters*, vol. 3, no. 9, pp. 1299-1304, 2003.doi:http://dx.doi.org/10.1021/nl034367o.

[3] L. Z. Lixin Dong, Dominik J. Bell, Bradley J. Nelson, Detlev Grützmacher, "Hybrid Nanorobotic Approaches for Fabricating NEMS," presented at the IEEE International Conference on Robotics and Automation, Orlando, 2006.doi:https://doi.org/10.1109/ROBOT.2006.1641904.

[4] Z. L. Xu D., Dong L., Nelson B.J. , *Encyclopedia of Nanotechnology*. Springer, 2012.doi:http://dx.doi.org/10.1007/978-90-481-9751-4.

[5] D. J. Bell, Y. Sun, L. Zhang, L. X. Dong, B. J. Nelson, and D. Grützmacher, "Three-dimensional nanosprings for electromechanical sensors," *Sensors and Actuators A: Physical*, vol. 130-131, pp. 54-61, 2006.doi:http://dx.doi.org/10.1016/j.sna.2005.10.057.

[6] B. H. Collins JA, Staab GH, *Mechanical design of machine elements and machines*, 2nd ed. Wiley, 2009.

[7] S. M. Kane JW, *Physics*, 3rd ed. Wiley, 1998.

[8] J. A. Rogers *et al.*, "Paper-like electronic displays: large-area rubber-stamped plastic sheets of electronics and microencapsulated electrophoretic inks," *Proc Natl Acad Sci U S A*, vol. 98, no. 9, pp. 4835-40, 2001.doi:https://doi.org/10.1073/pnas.091588098.

[9] V. L. Pushparaj *et al.*, "Flexible energy storage devices based on nanocomposite paper," *Proc Natl Acad Sci U S A*, vol. 104, no. 34, pp. 13574-7, 2007.doi:https://doi.org/10.1073/pnas.0706508104.

[10] S. Bauer, "Flexible electronics: Sophisticated skin," *Nat Mater* vol. 12, no. 10, pp. 871-872, 2013.doi:https://doi.org/10.1038/nmat3759.

[11] M. Melzer, Mönch, J. I., Makarov, D., Zabila, Y., Cañón Bermúdez, G. S., Karnaushenko, D., Baunack, S., Bahr, F., Yan, C., Kaltenbrunner, M., and Schmidt, O. G., "Wearable Magnetic Field Sensors for Flexible Electronics," *Adv Mater*, vol. 27, no. 7, pp. 1274-80, Feb 18 2015.doi:https://doi.org/10.1002/adma.201405027.

[12] Z. Chen, C. Xu, C. Ma, W. Ren, and H. M. Cheng, "Lightweight and flexible graphene foam composites for high-performance electromagnetic interference shielding," *Adv Mater*, vol. 25, no. 9, pp. 1296-300, 2013.doi:https://doi.org/10.1002/adma.201204196.

[13] L. Del Castillo *et al.*, "Flexible electronic assemblies for space applications," presented at the 2010 IEEE Aerospace Conference, 2010.doi:http://dx.doi.org/10.1109/aero.2010.5446717.

[14] S. Yao and Y. Zhu, "Nanomaterial-enabled stretchable conductors: strategies, materials and devices," *Adv Mater*, vol. 27, no. 9, pp. 1480-511, Mar 4 2015.doi:https://doi.org/10.1002/adma.201404446.

[15] H.-F. Zhang, C.-M. Wang, E. C. Buck, and L.-S. Wang, "Synthesis, Characterization, and Manipulation of Helical SiO2 Nanosprings," *Nano Letters*, vol. 3, no. 5, pp. 577-580, 2003.doi:http://dx.doi.org/10.1021/nl0341180.

[16] D. Zhang, A. Alkhateeb, H. Han, H. Mahmood, D. N. McIlroy, and M. G. Norton, "Silicon Carbide Nanosprings," *Nano Letters*, vol. 3, no. 7, pp. 983-987, 2003.doi:http://dx.doi.org/10.1021/nl034288c.

[17] D. N. McIlroy, D. Zhang, Y. Kranov, and M. G. Norton, "Nanosprings," *Applied Physics Letters*, vol. 79, no. 10, pp. 1540-1542, 2001.doi:10.1063/1.1400079.

[18] D. A. Antartis, R. N. Mott, and I. Chasiotis, "Silicon nanosprings fabricated by glancing angle deposition for ultra-compliant films and interfaces," *Materials and Design*, vol. 144, pp. 182-191, 2018.doi:http://dx.doi.org/10.1016/j.matdes.2018.02.017.

[19] S. Chen, H. Hou, P. Hu, J. H. Wendorff, A. Greiner, and S. Agarwal, "Polymeric Nanosprings by Bicomponent Electrospinning," *Macromolecular Materials and*

Engineering, vol. 294, no. 4, pp. 265-271, 2009.doi:http://dx.doi.org/10.1002/mame.200800342.

[20] S. Motojima, X. Chen, S. Yang, and M. Hasegawa, "Properties and potential applications of carbon microcoils/nanocoils," *Diamond and Related Materials*, vol. 13, no. 11-12, pp. 1989-1992, 2004.doi: https://doi.org/10.1016/j.diamond.2004.06.020.

[21] H. Ma, K. Nakata, L. Pan, K. Hirahara, and Y. Nakayama, "Relationship between the structure of carbon nanocoils and their electrical property," *Carbon*, vol. 73, pp. 71-77, 2014.doi: https://doi.org/10.1016/j.carbon.2014.02.038.

[22] K.-i. Nakamatsu, M. Nagase, J.-y. Igaki, H. Namatsu, and S. Matsui, "Mechanical characteristics and its annealing effect of diamondlike-carbon nanosprings fabricated by focused-ion-beam chemical vapor deposition," *Journal of Vacuum Science and Technology B: Microelectronics and Nanometer Structures*, vol. 23, no. 6, 2005.doi: https://doi.org/10.1116/1.2132329.

[23] T. Hayashida, L. Pan, and Y. Nakayama, "Mechanical and electrical properties of carbon tubule nanocoils," *Physica B: Condensed Matter*, vol. 323, no. 1-4, pp. 352-353, 2002.doi: https://doi.org/10.1016/s0921-4526(02)01002-5.

[24] C. Feng and K. M. Liew, "Structural stability of carbon nanosprings," *Carbon*, vol. 49, no. 14, pp. 4688-4694, 2011.doi: https://doi.org/10.1016/j.carbon.2011.06.066.

[25] M. A. Poggi *et al.*, "Measuring the Compression of a Carbon Nanospring," *Nano Letters*, vol. 4, no. 6, pp. 1009-1016, 2004.doi:https://doi.org/10.1021/nl0497023.

[26] T. Yonemura *et al.*, "Real-time deformation of carbon nanocoils under axial loading," *Carbon*, vol. 83, pp. 183-187, 2015.doi: https://doi.org/10.1016/j.carbon.2014.11.034.

[27] Y. Sun, C. Wang, L. Pan, X. Fu, P. Yin, and H. Zou, "Electrical conductivity of single polycrystalline-amorphous carbon nanocoils," *Carbon*, vol. 98, pp. 285-290, 2016.doi: https://doi.org/10.1016/j.carbon.2015.11.025.

[28] J. Zhao, J. Wu, J.-W. Jiang, L. Lu, Z. Zhang, and T. Rabczuk, "Thermal conductivity of carbon nanocoils," *Applied Physics Letters*, vol. 103, no. 23, 2013.doi: https://doi.org/10.1063/1.4839396.

[29] H. Ma, L. Pan, Q. Zhao, Z. Zhao, and J. Qiu, "Thermal conductivity of a single carbon nanocoil measured by field-emission induced thermal radiation," *Carbon*, vol. 50, no. 3, pp. 778-783, 2012.doi: https://doi.org/10.1016/j.carbon.2011.09.032.

[30] H. Raghubanshi, E. D. Dikio, and E. B. Naidoo, "The properties and applications of helical carbon fibers and related materials: A review," *Journal of Industrial and Engineering Chemistry*, vol. 44, pp. 23-42, 2016.doi: https://doi.org/10.1016/j.jiec.2016.08.023.

[31] L. Pan, T. Hayashida, M. Zhang, and Y. Nakayama, "Field Emission Properties of Carbon Tubule Nanocoils," *Japanese Journal of Applied Physics*, vol. 40, no. Part 2, No. 3B, pp. L235-L237, 2001.doi: https://doi.org/10.1143/jjap.40.L235.

[32] S. Hokushin, L. Pan, Y. Konishi, H. Tanaka, and Y. Nakayama, "Field Emission Properties and Structural Changes of a Stand-Alone Carbon Nanocoil," *Japanese Journal of Applied Physics*, vol. 46, no. No. 23, pp. L565-L567, 2007.doi: https://doi.org/10.1143/jjap.46.L565.

[33] T. Y. e. al, "Torsion fracture of carbon nanocoils," *Journal of Applied Physics*, vol. 112, no. 8, 2012.doi:https://doi.org/10.1063/1.4758921.

[34] M. e. al., "Properties and potential applications of carbon microcoils/nanocoils," *Diamond and Related Materials*, vol. 13, no. 11-12, pp. 1989-1992, 2004.doi:https://doi.org/10.1016/j.diamond.2004.06.020.

[35] K. Yoshimura, K. Nakano, T. Miyake, Y. Hishikawa, and S. Motojima, "Effectiveness of carbon microcoils as a reinforcing material for a polymer matrix," *Carbon*, vol. 44, no. 13, pp. 2833-2838, 2006.doi:https://doi.org/10.1016/j.carbon.2006.03.021.

[36] X.-L. Wu, Q. Liu, Y.-G. Guo, and W.-G. Song, "Superior storage performance of carbon nanosprings as anode materials for lithium-ion batteries,"

Electrochemistry Communications, vol. 11, no. 7, pp. 1468-1471, 2009.doi: https://doi.org/10.1016/j.elecom.2009.05.033.

[37] Y. Kato, N. Adachi, T. Okuda, T. Yoshida, S. Motojima, and T. Tsuda, "Evaluation of Induced Electromotive Force of a Carbon Micro Coil*," *Japanese Journal of Applied Physics*, vol. 42, no. Part 1, No. 8, pp. 5035-5037, 2003.doi:https://doi.org/10.1143/JJAP.42.5035.

[38] K. Yamamoto, T. Hirayama, M. Kusunoki, S. Yang, and S. Motojima, "Electron holographic observation of micro-magnetic fields current-generated from single carbon coil," *Ultramicroscopy*, vol. 106, no. 4-5, pp. 314-9, Mar 2006.doi:https://doi.org/10.1016/j.ultramic.2005.10.002.

[39] S. Yang, X. Chen, H. Aoki, and S. Motojima, "Tactile microsensor elements prepared from aligned superelastic carbon microcoils and polysilicone matrix," *Smart Materials and Structures*, vol. 15, no. 3, pp. 687-694, 2006.doi: https://doi.org/10.1088/0964-1726/15/3/003.

[40] S. H. S. Motojimaa , Y. Hishikawa, "Electromagnetic wave absorption properties of carbon microcoils /PMMA composite beads in W bands," *Carbon*, vol. 41, pp. 2653-2689, 2003.doi:https://doi.org/10.1016 /S0008-6223(03)00292-6.

[41] D.-L. Zhao and Z.-M. Shen, "Preparation and microwave absorption properties of carbon nanocoils," *Materials Letters*, vol. 62, no. 21-22, pp. 3704-3706, 2008.doi: https://doi.org/10.1016/j.matlet.2008.04.032.

[42] N. Tang *et al.*, "Synthesis, Microwave Electromagnetic, and Microwave Absorption Properties of Twin Carbon Nanocoils," *The Journal of Physical Chemistry C*, vol. 112, no. 49, pp. 19316-19323, 2008.doi:https://doi.org/10.1021/jp808087n.

[43] L. Liu, K. Zhou, P. He, and T. Chen, "Synthesis and microwave absorption properties of carbon coil–carbon fiber hybrid materials," *Materials Letters*, vol. 110, pp. 76-79, 2013.doi: https://doi.org/10.1016/j.matlet.2013.07.131.

[44] S. Motojima, M. Kawaguchi, K. Nozaki, and H. Iwanaga, "Growth of regularly coiled carbon filaments by Ni catalyzed pyrolysis of acetylene, and their

morphology and extension characteristics," *Applied Physics Letters*, vol. 56, no. 4, pp. 321-323, 1990.doi:https://doi.org/10.1063/1.102816.

[45] S. Motojima, I. Hasegawa, S. Kagiya, M. Momiyama, M. Kawaguchi, and H. Iwanaga, "Preparation of coiled carbon fibers by pyrolysis of acetylene using a Ni catalyst and sulfur or phosphorus compound impurity," *Applied Physics Letters*, vol. 62, no. 19, pp. 2322-2323, 1993.doi: https://doi.org/10.1063/1.109634.

[46] V. K. Varadan, R. D. Hollinger, V. V. Varadan, J. Xie, and P. K. Sharma, "Development and characterization of micro-coil carbon fibers by a microwave CVD system," *Smart Materials and Structures*, vol. 9, no. 4, pp. 413-420, 2000.doi:http://dx.doi.org/10.1088/0964-1726/9/4/304.

[47] W. I.-H. Chihiro Kuzuya, Shinji Hirako, Yukio Hishikawa, Seiji Motojima, "Preparation, Morphology, and Growth Mechanism of Carbon Nanocoils," *Chemical Vapor Deposition*, vol. 8, no. 2, pp. 57-62, 2002.doi:https://doi.org/10.1002/1521-3862(20020304)8:2%3C57::AID-CVDE57%3E3.0.CO;2-Y.

[48] Y. Qin, Z. Zhang, and Z. Cui, "Helical carbon nanofibers with a symmetric growth mode," *Carbon*, vol. 42, no. 10, pp. 1917-1922, 2004.doi:https://doi.org/10.1016/j.carbon.2004.03.020.

[49] S. Yang, X. Chen, S. Motojima, and M. Ichihara, "Morphology and microstructure of spring-like carbon micro-coils/nano-coils prepared by catalytic pyrolysis of acetylene using Fe-containing alloy catalysts," *Carbon*, vol. 43, no. 4, pp. 827-834, 2005.doi:https://doi.org/10.1016/j.carbon.2004.11.014.

[50] W. Wang, K. Yang, J. Gaillard, P. R. Bandaru, and A. M. Rao, "Rational Synthesis of Helically Coiled Carbon Nanowires and Nanotubes through the Use of Tin and Indium Catalysts," *Advanced Materials*, vol. 20, no. 1, pp. 179-182, 2008.doi:https://doi.org/10.1002/adma.200701143.

[51] A. Shaikjee and N. J. Coville, "The synthesis, properties and uses of carbon materials with helical morphology," *Journal of Advanced Research,* vol. 3, no. 3, pp. 195-223, 2012.doi:https://doi.org/10.1016/j.jare.2011.05.007.

[52] G. Wang *et al.*, "Size-selective catalytic growth of nearly 100% pure carbon nanocoils with copper nanoparticles produced by atomic layer deposition," *ACS Nano,* vol. 8, no. 5, pp. 5330-8, May 27 2014.doi:https://doi.org/10.1021/nn501709h.

[53] W. Wang, K. Q. Yang, J. Gaillard, P. R. Bandaru, and A. M. Rao, "Rational synthesis of helically coiled carbon nanowires and nanotubes through the use of tin and indium catalysts," (in English), *Advanced Materials,* vol. 20, no. 1, pp. 179-+, Jan 7 2008.doi:10.1002/adma.200701143.

[54] M. M. Hasan, Y. Zhou, and S. Jeelani, "Thermal and tensile properties of aligned carbon nanofiber reinforced polypropylene," *Materials Letters,* vol. 61, no. 4-5, pp. 1134-1136, 2007.doi:http://dx.doi.org/10.1016/j.matlet.2006.06.074.

[55] R. J. Kuriger, M. K. Alam, D. P. Anderson, and R. L. Jacobsen, "Processing and characterization of aligned vapor grown carbon fiber reinforced polypropylene," *Composites Part A: Applied Science and Manufacturing,* vol. 33, no. 1, pp. 53-62, 2002.doi:http://dx.doi.org/10.1016/s1359-835x(01)00070-7.

[56] C.-S. Lim, A. J. Rodriguez, M. E. Guzman, J. D. Schaefer, and B. Minaie, "Processing and properties of polymer composites containing aligned functionalized carbon nanofibers," *Carbon,* vol. 49, no. 6, pp. 1873-1883, 2011.doi:http://dx.doi.org/10.1016/j.carbon.2011.01.010.

[57] J. Cai, S. Chawla, and M. Naraghi, "Microstructural evolution and mechanics of hot-drawn CNT-reinforced polymeric nanofibers," *Carbon,* vol. 109, pp. 813-822, 2016.doi:http://dx.doi.org/10.1016/j.carbon.2016.08.080.

[58] S. Chawla, J. Cai, and M. Naraghi, "Mechanical tests on individual carbon nanofibers reveals the strong effect of graphitic alignment achieved via precursor hot-drawing," *Carbon,* vol. 117, pp. 208-219, 2017.doi:http://dx.doi.org/10.1016/j.carbon.2017.02.095.

[59] M. I. Darby and V. N. Kanellopoulos, "Theory of fibre buckling in carbon-fibre reinforced plastics," *Journal of Physics D: Applied Physics,* vol. 20, no. 3, pp. 298-302, 1987.doi:http://dx.doi.org/10.1088/0022-3727/20/3/009.

[60] C. Mueller, A. Gorius, S. Nazarenko, A. Hiltner, and E. Baer, "Single Fiber Microbuckling in a Model Composite," *Journal of Composite Materials,* vol. 30, no. 17, pp. 1912-1921, 1996.doi: https://doi.org/10.1177/002199839603001703.

[61] V. Slesarenko and S. Rudykh, "Microscopic and macroscopic instabilities in hyperelastic fiber composites," *Journal of the Mechanics and Physics of Solids,* vol. 99, pp. 471-482, 2017.doi: https://doi.org/10.1016/j.jmps.2016.11.002.

[62] Y. Chen, Y. Liu, Y. Yan, Y. Zhu, and X. Chen, "Helical coil buckling mechanism for a stiff nanowire on an elastomeric substrate," *Journal of the Mechanics and Physics of Solids,* vol. 95, pp. 25-43, 2016.doi: https://doi.org/10.1016/j.jmps.2016.05.020.

[63] P. Ciarletta and M. Destrade, "Torsion instability of soft solid cylinders," *IMA Journal of Applied Mathematics,* vol. 79, no. 5, pp. 804-819, 2014.doi:http://dx.doi.org/10.1093/imamat/hxt052.

[64] S. Mora, M. Abkarian, H. Tabuteau, and Y. Pomeau, "Surface instability of soft solids under strain," *Soft Matter,* vol. 7, no. 22, 2011.doi:http://dx.doi.org/10.1039/c1sm06051a.

[65] J. Bicerano, *Prediction of polymer properties* (Plastics engineering). Marcel Dekker, 2002, p. 746.

[66] F.Chen, " A constitutive model of polyether-ether-ketone (PEEK)," Journal of the Mechanical Behavior of Biomedical Materials, vol. 53, pp. 427-433, 2016.doi: http://dx.doi.org/10.1016/j.jmbbm.2015.08.037.

[67] S. Khatri, J. Cai and M. Naraghi," Formation of wavy carbon nanofibers and nanocoils via precursor constrained microbuckling," *Journal of the Mechanics and Physics of Solids,* vol. 134, pp. 103763, 2019.doi: https://doi.org/10.1016/j.jmps.2019.103763